Genes Affecting Vocal and Facial Anatomy Went Through Extensive Regulatory Divergence in Modern Humans

David Gokhman[1,*], Malka Nissim-Rafinia[1], Lily Agranat-Tamir[1,2], Genevieve Housman[3,4], Raquel García-Pérez[5], Esther Lizano[5], Olivia Cheronet[6], Swapan Mallick[7,8,9], Maria A. Nieves-Colón[3,4], Heng Li[7], Songül Alpaslan-Roodenberg[8], Mario Novak[10,11], Hongcang Gu[7], Jason M. Osinski[12], Manuel Ferrando-Bernal[5], Pere Gelabert[5], Iddi Lipende[13], Deus Mjungu[13], Ivanela Kondova[14], Ronald Bontrop[14], Ottmar Kullmer[15], Gerhard Weber[6], Tal Shahar[16], Mona Dvir-Ginzberg[17], Marina Faerman[18], Ellen E. Quillen[19], Alexander Meissner[7,20,21], Yonatan Lahav[22], Leonid Kandel[23], Meir Liebergall[23], María E. Prada[24], Julio M. Vidal[25], Richard M. Gronostajski[12,26], Anne C. Stone[3,4,27],Benjamin Yakir[2], Carles Lalueza-Fox[5], Ron Pinhasi[6], David Reich[7,8,9], Tomas Marques-Bonet[5,28,29,30], Eran Meshorer[1,31,*], Liran Carmel[1,*]

[1] Department of Genetics, The Alexander Silberman Institute of Life Sciences, Faculty of Science, The Hebrew University of Jerusalem, Edmond J. Safra Campus, Givat Ram, Jerusalem 91904, Israel.
[2] Department of Statistics, The Hebrew University of Jerusalem, Jerusalem 91905, Israel.
[3] School of Human Evolution and Social Change, Arizona State University, Tempe, AZ 85281, USA.
[4] Center for Evolution and Medicine, Arizona State University, Tempe, AZ 85287, USA.
[5] Institute of Evolutionary Biology (UPF-CSIC), PRBB, Dr. Aiguader 88, 08003 Barcelona, Spain.
[6] Department of Evolutionary Anthropology. University of Vienna, Althanstrasse 14, 1090 Vienna, Austria
[7] Broad Institute, Cambridge MA 02138, USA.
[8] Department of Genetics, Harvard Medical School, Boston, MA 02115, USA.
[9] Howard Hughes Medical Institute, Harvard Medical School, Boston, MA 02115, USA.
[10] Institute for Anthropological Research, Ljudevita Gaja 32, 10000 Zagreb, Croatia.
[11] Earth Institute and School of Archaeology, University College Dublin, Dublin 4, Ireland.
[12] Department of Biochemistry, Jacobs School of Medicine and Biomedical Sciences, University at Buffalo, Buffalo NY, 14203
[13] Gombe Stream Research Center, Jane Goodall Institute, Kigoma, Tanzania.
[14] Biomedical Primate Research Centre (BPRC), Rijswijk, The Netherlands.

[15] Department of Palaeoanthropology and Messel Research, Senckenberg Center of Human Evolution and Paleoecology, Frankfurt am Main, Germany
[16] Department of Neurosurgery, Shaare Zedek Medical Center, Jerusalem, Israel.
[17] Laboratory of Cartilage Biology, Institute of Dental Sciences, Faculty of Dental Medicine, Hebrew University of Jerusalem, PO BOX 12272, Ein Kerem Campus, Jerusalem 91120, Israel
[18] Laboratory of Bioanthropology and Ancient DNA, Institute of Dental Sciences, Faculty of Dental Medicine, The Hebrew University of Jerusalem, PO BOX 12272, Ein Kerem Campus, Jerusalem 91120, Israel.
[19] Department of Genetics, Texas Biomedical Research Institute, San Antonio, Texas 85287, USA.
[20] Harvard Stem Cell Institute, Cambridge, MA 02138 USA.
[21] Department of Stem Cell and Regenerative Biology, Harvard University, Cambridge, MA 02138 USA
[22] Otolaryngology - Head & Neck surgery department, Laryngeal surgery unit. Kaplan medical center, Rehovot, Israel. Affiliated with the Hebrew University Medical School, Jerusalem, Israel.
[23] Orthopaedic Department, Hadassah – Hebrew University Medical Center, Jerusalem, Israel.
[24] I.E.S.O. 'Los Salados'. Junta de Castilla y León, Spain.
[25] Junta de Castilla y León, Servicio de Cultura de León, Spain.
[26] Genetics, Genomics and Bioinformatics Program, New York State Center of Excellence in Bioinformatics and Life Sciences, Jacobs School of Medicine and Biomedical Sciences, University at Buffalo, Buffalo NY, 14203
[27] Institute of Human Origins, Arizona State University, Tempe, AZ 85287, USA.
[28] Catalan Institution of Research and Advanced Studies (ICREA), Passeig de Lluís Companys, 23, 08010 Barcelona, Spain.
[29] CNAG-CRG , Centre for Genomic Regulation (CRG), Barcelona Institute of Science and Technology (BIST), Baldiri i Reixac 4, 08028 Barcelona, Spain.
[30] Institut Català de Paleontologia Miquel Crusafont, Universitat Autònoma de Barcelona, Edifici ICTA-ICP, c/ Columnes s/n, 08193 Cerdanyola del Vallès, Barcelona, Spain
[31] The Edmond and Lily Safra Center for Brain Sciences (ELSC), The Hebrew University of Jerusalem, Edmond J. Safra Campus, Givat Ram, Jerusalem, 91904, Israel.

Corresponding authors: David Gokhman (David.gokhman@mail.huji.ac.il), Eran Meshorer (eran.meshorer@mail.huji.ac.il), and Liran Carmel (liran.carmel@huji.ac.il)

Summary

Regulatory changes are broadly accepted as key drivers of phenotypic divergence. However, identifying regulatory changes that underlie human-specific traits has proven very challenging. Here, we use 63 DNA methylation maps of ancient and present-day humans, as well as of six chimpanzees, to detect differentially methylated regions that emerged in modern humans after the split from Neanderthals and Denisovans. We show that genes affecting the face and vocal tract went through particularly extensive methylation changes. Specifically, we identify widespread hypermethylation in a network of face- and voice-affecting genes (*SOX9*, *ACAN*, *COL2A1*, *NFIX* and *XYLT1*). We propose that these repression patterns appeared after the split from Neanderthals and Denisovans, and that they might have played a key role in shaping the modern human face and vocal tract.

Keywords: Epigenetics, Paleoepigenetics, aDNA, Neandertal, Denisova, Gene regulation, Craniofacial morphology, Larynx, Vocal cords, Voice box

71 # Introduction

72 The advent of high-coverage ancient genomes of archaic humans (Neanderthal and Denisovan)
73 introduced the possibility to identify the genetic basis of some unique modern human traits[1]. A
74 common approach is to carry out sequence comparisons and detect non-neutral sequence
75 changes. However, out of ~30,000 substitutions and indels that reached fixation in modern
76 humans, less than 100 directly alter amino acid sequence[1], and as of today, our ability to estimate
77 the biological effects of the remaining ~30,000 noncoding changes is very restricted. Whereas
78 many of them are probably nearly neutral, many others may affect gene function, especially
79 those in regulatory regions such as promoters and enhancers. Such regulatory changes may have
80 a sizeable impact on human evolution, as alterations in gene regulation are thought to underlie
81 much of the phenotypic variation between closely related groups[2]. Because of the limited ability
82 to interpret noncoding variants, direct examination of regulatory layers such as DNA methylation
83 has the potential to enhance our understanding of the evolutionary origin of human-specific traits
84 far beyond what can be achieved using sequence comparison alone[3].
85 In order to gain insight into the regulatory changes that underlie human evolution, we previously
86 developed a method to reconstruct DNA methylation maps of ancient genomes based on analysis
87 of patterns of damage to ancient DNA[4]. We used this method to reconstruct the methylomes of a
88 Neanderthal and a Denisovan, which were then compared to a partial methylation map of a
89 present-day osteoblast cell line. However, the ability to identify differentially methylated regions
90 (DMRs) between the human groups was constrained by the incomplete reference map (providing
91 methylation information for ~10% of CpG sites), differences in outputs of sequencing platforms,
92 lack of an outgroup, and a restricted set of skeletal samples (see Methods).

93 To study the evolutionary dynamics of DNA methylation along the hominin tree on a larger
94 scale, we establish here the most comprehensive assembly to date of skeletal DNA methylation
95 maps from modern humans, archaic humans, and chimpanzees. Using these maps, we identify
96 588 genes whose methylation state is unique to modern human. We then analyze the function of
97 these genes by investigating their known anatomical effects, and validate this using over 50
98 orthogonal tests and controls. We find that the most extensive DNA methylation changes are
99 observed in genes that affect vocal and facial anatomy, and that this trend is unique to modern
100 humans.

101 Results

102 We reconstructed ancient DNA methylation maps of eight individuals: in addition to the
103 previously published Denisovan and Altai Neanderthal methylation maps[4], we reconstructed the
104 methylomes of the Vindija Neanderthal (~52 thousand years ago, kya)[5], and three anatomically
105 modern humans: the Ust'-Ishim individual (~45 kya, Western Siberia)[6], the Loschbour individual
106 (~8 kya, Luxemburg)[7], and the Stuttgart individual (~7 kya, Germany)[7]. We also sequenced to
107 high-coverage and reconstructed the methylomes of the La Braña 1 individual from Spain (~8
108 kya, 22x) (which was previously sequenced to low-coverage[8]) and an individual from Barçın
109 Höyük, Western Anatolia, Turkey (I1583, ~8.5 kya, 24x), which was previously sequenced using
110 a capture array[9].
111 To this set we added 52 publicly available partial bone methylation maps from present-day
112 individuals, produced using 450K methylation arrays (see Methods). To obtain full present-day
113 bone maps, we produced whole-genome bisulfite sequencing (WGBS) methylomes from the
114 femur bones of two individuals (Bone1 and Bone2). Hereinafter, ancient and present-day modern

115 humans are collectively referred to as *anatomically modern humans* (AMHs), while the
116 Neanderthal and Denisovan are referred to as *archaic humans*. As an outgroup, we produced
117 methylomes of six chimpanzees: one WGBS, one reduced representation bisulfite sequencing
118 (RRBS) and four 850K methylation arrays. Together, these data establish a unique and
119 comprehensive platform to study DNA methylation dynamics in recent human evolution
120 (Extended Data Table 1).

121 **Identification of DMRs**

122 We developed a DMR-detection method for ancient methylomes, which accounts for potential
123 noise introduced during reconstruction, as well as differences in coverage and deamination rates
124 (Extended Data Fig. 1). To minimize the number of false positives and to identify DMRs that are
125 most likely to have a regulatory effect, we applied a strict threshold of >50% difference in
126 methylation across a minimum of 50 CpGs. This also filters out environmentally-induced DMRs
127 which typically show small methylation differences and limited spatial scope[10]. Using this
128 method, we identified 9,679 regions overall that showed methylation differences between any of
129 the high-quality representative methylomes of the Denisovan, the Altai Neanderthal, and the
130 Ust'-Ishim anatomically modern human. These regions do not necessarily represent evolutionary
131 differences between the human groups. Rather, many of them could be attributed to factors
132 separating the three individuals (e.g., Ust'-Ishim is a male whereas the archaic humans are
133 females), or to variability within populations. To minimize such effects, we used the 59
134 additional human maps to filter out regions where variability in methylation is detected. We
135 adopted a conservative approach, whereby we take only loci where methylation in one hominin
136 group is found completely outside the range of methylation in the other groups (Fig. 1a).
137 Importantly, our samples come from both sexes, from individuals of various ages and ancestries,

138 from sick and healthy individuals, and from a variety of skeletal parts (femur, skull, phalanx,
139 tooth, and rib). Hence, this procedure is expected to account for these potentially confounding
140 factors, and the remaining DMRs are expected to represent true evolutionary differences (Fig.
141 1a-c, Extended Data Fig. 1, see Methods). This step resulted in a set of 7,649 DMRs that
142 discriminate between the human groups, which we ranked according to their significance level.
143 Next, using the chimpanzee samples, we were able to determine for 2,825 of these DMRs the
144 lineage where the methylation change occurred (Fig. 1d). Of these DMRs, 873 are AMH-
145 derived, 939 are archaic-derived, 443 are Denisovan-derived, and 570 are Neanderthal-derived
146 (Fig. 2a, Extended Data Fig. 1, Extended Data Table 2). To study the derived biology of
147 AAMHs, and to focus on DMRs that are based on the most extensive set of maps, we
148 concentrated on the 873 AMH-derived DMRs. We found that these DMRs are located 58x closer
149 to AMH-derived sequence changes than expected by chance (0.092 Mb vs. a median of 5.3 Mb,
150 $P < 10^{-5}$, permutation test, Fig. 2b). This suggests that some of the methylation changes might
151 have been driven by cis-regulatory sequence variants that arose along the AMH lineage.

152 **Face and voice-affecting genes are derived in AMHs**

153 We defined differentially methylated genes (DMGs) as genes that overlap at least one DMR
154 along their body or in their promoter, up to 5 kb upstream. The 873 AMH-derived DMRs are
155 linked to 588 AMH-derived DMGs (Extended Data Table 2). To gain insight into the function of
156 these DMGs, we first analyzed their gene ontology (GO). As expected from genes that show
157 differential methylation in the skeleton between human groups, AMH-derived DMGs are
158 enriched with terms associated with the skeleton (e.g., *endochondral bone morphogenesis,*
159 *trabecula morphogenesis,* and *palate development*). Also notable are terms associated with the
160 skeletal muscular, cardiovascular, and nervous systems (Extended Data Table 3).

161 To acquire a more precise understanding of the possible functional consequences of these
162 DMGs, we used Gene ORGANizer, which links human genes to the organs they phenotypically
163 affect[11]. Unlike tools that use GO terms or RNA expression data, Gene ORGANizer is based
164 entirely on curated gene-disease and gene-phenotype associations from monogenic diseases. It
165 relies on direct phenotypic observations in human patients whose conditions result from known
166 gene perturbations. Using Gene ORGANizer, we found 11 organs that are over-represented
167 within the 588 AMH-derived DMGs, eight of which are skeletal parts that can be divided into
168 three regions: the face, larynx (voice box), and pelvis (Fig. 2c, Extended Data Table 4). The
169 strongest enrichment was observed in the laryngeal region (x2.11 and x1.68, FDR = 0.017 and
170 0.048, for the vocal folds (vocal cords) and larynx, respectively), followed by facial and pelvic
171 structures, including the teeth, forehead, jaws, and pelvis. Interestingly, the face and pelvis are
172 considered the most morphologically divergent regions between Neanderthals and AMHs[12] and
173 our results reflect this divergence through gene regulation changes. To gain orthogonal evidence
174 for the enrichment of the larynx and face within these AMH-derived DMGs, we carried out a
175 number of additional analyses: First, we analyzed gene expression patterns and found that the
176 supralaryngeal vocal tract (the pharyngeal, oral, and nasal cavities, where sound is filtered to
177 specific frequencies) is the most enriched body part (1.7x and 1.6x, FDR = 5.6×10^{-6} and FDR =
178 7.3×10^{-7}, for the pharynx and larynx, respectively, Extended Data Table 3). Second, 44 of the
179 AMH-derived DMRs overlap previously reported putative enhancers of human craniofacial
180 developmental genes (5.1x compared to expected, $P < 10^{-4}$, permutation test)[13,14]. Third, *Palate*
181 *development* is the third most enriched GO term among AMH-derived DMGs (Extended Data
182 Table 3). Fourth, DMGs significantly overlap genes associated with craniofacial features in the
183 GWAS catalog[15] ($P = 3.4 \times 10^{-4}$, hypergeometric test).

184 To test whether this enrichment remains if we take only the most confident DMRs, we limited
185 the analysis to DMGs where the most significant DMRs are found (top quartile, Q statistic).
186 Here, the over-representation of voice-affecting genes is even more pronounced (2.82x and
187 2.26x, for vocal folds and larynx, respectively, FDR = 0.028 for both, Fig. 2d, Extended Data
188 Table 4). Hereinafter, we refer to genes as affecting an organ if they have been shown to have a
189 phenotypic effect on that organ in some or all patients where this gene is dysfunctional.
190 Next, we reasoned that skeleton-associated genes might be over-represented in analyses that
191 compare bone DNA methylation maps, hence introducing potential biases. To test whether this
192 enrichment might explain the over-representation of the larynx, face, and pelvis, we compared
193 the fraction of genes affecting these organs within all skeletal genes to their fraction within the
194 skeletal genes in the AMH-derived DMGs. We found that genes affecting the face, larynx, and
195 pelvis are significantly over-represented even within skeletal AMH-derived DMGs ($P = 1.0 \times 10^{-}$
196 ^{5}, $P = 1.3 \times 10^{-3}$, $P = 2.1 \times 10^{-3}$, $P = 0.03$, for vocal folds, larynx, face, and pelvis, respectively,
197 hypergeometric test). Additionally, using a permutation test, we found that the enrichment levels
198 within AMH-derived DMGs are significantly higher than expected by chance for the laryngeal
199 and facial regions, but not for the pelvis ($P = 8.0 \times 10^{-5}$, $P = 3.6 \times 10^{-3}$, $P = 8.2 \times 10^{-4}$, and $P =$
200 0.115, for vocal folds, larynx, face and pelvis, respectively, Extended Data Fig. 2b-e, see
201 Methods). Thus, we found that the enrichment in the facial and laryngeal regions is not a by-
202 product of a general enrichment in skeletal parts, and we hereinafter focus on genes affecting
203 these two regions.
204 Finally, we ruled out the options that our DMR-detection algorithm, number of samples, filtering
205 process or biological factors such as gene length, cellular composition, pleiotropy or
206 developmental stage might underlie the enrichment of these organs (see Methods).

207 Perhaps most importantly, none of the other branches shows enrichment of the larynx or the
208 vocal folds; Neanderthal- and Denisovan-derived DMGs show no significant enrichment in any
209 organ, and archaic-derived DMGs are over-represented in the jaws, lips, limbs, scapulae, and
210 spinal column, but not in the larynx or vocal folds (Extended Data Fig. 2f, Extended Data Table
211 4). In addition, DMRs that separate chimpanzees from all humans (archaic and modern,
212 Extended Data Table 2) do not show enrichment of genes affecting the larynx or face,
213 compatible with the notion that this trend emerged along the AMH lineage.
214 Taken together, we conclude that DMGs that emerged along the AMH lineage are uniquely
215 enriched in genes affecting the voice and face, and that this is unlikely to be an artifact of (a)
216 inter-individual variability resulting from age, sex, disease, or bone type; (b) significance level of
217 DMRs; (c) the reconstruction or DMR-detection processes; (d) number of samples used; (e)
218 pleiotropic effects; (f) the types of methylation maps used; (g) the comparison of skeletal
219 methylomes; (h) gene length distribution; or (i) biological factors such as cellular composition
220 and developmental state.
221 Our analyses identified 56 DMRs in genes affecting the facial skeleton, and 32 in genes affecting
222 the laryngeal skeleton. The face-affecting genes are known to shape mainly the protrusion of the
223 lower and midface, the size of the nose, and the slope of the forehead. Interestingly, these traits
224 are considered some of the most derived between Neanderthals and AMHs[12]. The larynx-
225 affecting genes have been shown to underlie various phenotypes in patients, ranging from slight
226 changes to the pitch and hoarseness of the voice, to a complete loss of speech ability[11] (Extended
227 Data Table 5). These phenotypes were shown to be driven primarily by alterations to the
228 laryngeal and vocal tract skeleton. Methylation patterns in differentiated cells are often
229 established during earlier stages of development, and the closer two tissues are developmentally,

230 the higher the similarity between their methylation maps[3,16,17]. This is also evident in the fact that
231 DMRs identified between species in one tissue often exist in other tissues as well[16]. Importantly,
232 the laryngeal skeleton, and particularly the arytenoid cartilage to which the vocal folds are
233 anchored, share an origin from the somatic layer of the lateral plate mesoderm with the
234 cartilaginous tissue of the limb bones prior to their ossification. Thus, it is likely that many of the
235 DMRs identified here between limb samples also exist in their closest tissue – the laryngeal
236 skeleton. This is further supported by the observation that these DMGs are consistent across all
237 examined skeletal samples, including skull, femur, rib, tibia, and tooth. Furthermore, we directly
238 measured methylation levels in a subset of the DMRs in primary chondrocytes and show that
239 their patterns extend to these cells as well (see below).

240 **Extensive methylation changes within face and voice-affecting genes**

241 The results above suggest that methylation levels in many face- and voice-affecting genes have
242 changed in AMHs since the split from archaic humans, but they do not provide information on
243 the extent of changes within each gene. To do so, we scanned the genome in windows of 100 kb
244 and computed the fraction of CpGs which are differentially methylated in AMHs (hereinafter,
245 AMH-derived CpGs). We found that the extent of changes within voice-affecting DMGs is most
246 profound, more than 2x compared to other DMGs (0.132 vs. 0.055, FDR = 2.3×10^{-3}, *t*-test,
247 Extended Data Table 6). Face-affecting DMGs also present high density of AMH-derived CpGs
248 (0.079 vs. 0.055, FDR = 2.8×10^{-3}). In archaic-derived DMGs, on the other hand, the extent of
249 changes within voice- and face-affecting genes is not different than expected (FDR = 0.99,
250 Extended Data Table 6). To control for possible biases, we repeated the analysis using only the
251 subset of DMRs in genes affecting the skeleton. Here too, we found that voice-affecting AMH-
252 derived DMGs present the highest density of changes (2.5x for vocal folds, 2.4x for larynx, FDR

253 = 1.4 x 10^{-3} for both, Extended Data Table 6), and face-affecting DMGs also exhibit a
254 significantly elevated density of changes (1.4x, FDR = 0.04).
255 We also found that compared to other AMH-derived DMRs, DMRs in voice- and face-affecting
256 genes tend to be 40% closer to candidate positively selected loci in AMHs[18] ($P < 10^{-4}$,
257 permutation test).
258 Strikingly, when ranking DMGs according to the fraction of AMH-derived CpGs, all top five
259 skeleton-related DMGs (*ACAN*, *SOX9*, *COL2A1*, *XYLT1*, and *NFIX*) are known to affect lower
260 and midfacial protrusion, as well as the voice[11,19] (Fig. 3a,b, Extended Data Fig. 2g). This is
261 particularly surprising considering that genome-wide, less than 2% of genes (345) are known to
262 affect the voice, ~3% of genes (726) are known to affect lower and midfacial protrusion, and less
263 than 1% (182) are known to affect both[11,19].
264 The three skeletal DMGs with the highest density of AMH-derived CpGs are the extra-cellular
265 matrix genes *ACAN* and *COL2A1,* and their key regulator *SOX9*, which together form a network
266 that regulates skeletal growth, the transition from cartilage to bone, and spatio-temporal
267 patterning of skeletal development, including the facial and laryngeal skeleton in humans[19,20] and
268 mouse[21]. *SOX9* was also shown to be one of the top genes underlying variation in craniofacial
269 morphology within-AMHs[22]. *SOX9* is regulated by a series of upstream enhancers identified in
270 mouse and human[23]. In human skeletal samples, hypermethylation of the *SOX9* promoter was
271 shown to down-regulate its activity, and consequently its targets[24]. This was also demonstrated
272 repeatedly in non-skeletal tissues of human[25,26] and mouse[27,28]. We found substantial
273 hypermethylation in AMHs in the following regions: (a) the *SOX9* promoter; (b) seven of its
274 proximal and distal skeletal and skeletal progenitor enhancers[23]; (c) the targets of SOX9: *ACAN*
275 (DMR #80) and *COL2A1* (DMR #1, the most significant AMH-derived DMR, which spans 32kb

276 and covers almost the entire *COL2A1* gene, from its 1st intron to its 54th exon and 3'UTR
277 region); and (d) an upstream lincRNA (*LINC02097*). Notably, regions (a), (b), and (d) overlap
278 the longest DMR on the AMH-derived DMR list, spanning 35,910 bp (DMR #11, Fig. 4).
279 Additionally, a more distant putative enhancer, located 345 kb upstream of *SOX9*, was shown to
280 bear strong active histone modification marks in chimpanzee craniofacial progenitor cells;
281 whereas, in humans these marks are almost absent (~10x lower than chimpanzee, suggesting
282 down-regulation, Fig. 4b)[13]. Importantly, human and chimpanzee non-skeletal tissues (i.e., brain
283 and blood) exhibit very similar methylation patterns in these genes, suggesting the DMRs are
284 skeleton-specific. Finally, the amino acid sequence coded by each of these genes is identical
285 across the hominin groups[1], suggesting that the observed changes are purely regulatory.
286 Together, these observations support the idea that *SOX9* became down-regulated in AMH
287 skeletal tissues, likely followed by down-regulation of its targets: *ACAN* and *COL2A1*.
288 *XYLT1*, the 4th highest skeleton-related DMG, is an enzyme involved in the synthesis
289 of glycosaminoglycan. Loss-of-function mutations, hypermethylation of the gene and its
290 consequent reduced expression underlie the Desbuquois dysplasia skeletal syndrome, which was
291 shown to affect the cartilaginous structure of the larynx, and drive a retraction of the face[29,30].
292 Very little is known about *XYLT1* regulation, but interestingly, in zebrafish it was shown to be
293 bound by SOX9 [[31]].
294 To quantitatively investigate the potential phenotypic consequences of these DMGs, we tested
295 what fraction of their known phenotypes are also known as traits that differ between modern and
296 archaic humans. We found that four of the top five most differentially methylated genes (*XYLT1*,
297 *NFIX*, *ACAN*, and *COL2A1*) are in the top 100 genes with the highest fraction of divergent traits
298 between Neanderthals and AMHs. Remarkably, *COL2A1*, the most divergent gene in its

299 methylation patterns, is also the most divergent in its phenotypes: no other gene in the genome is
300 associated with as many divergent traits between modern humans and Neanderthals (63 traits,
301 Extended Data Table 7, see Methods). This suggests that these extensive methylation changes
302 are possibly linked to phenotypic divergence between archaic and AMHs.

303 ## *NFIX* methylation patterns suggest downregulation in AMHs

304 In order to investigate how methylation changes affect expression levels, we scanned the DMRs
305 to identify those whose methylation levels are strongly correlated with expression across 22
306 human tissues[32]. We found 90 such AMH-derived DMRs (FDR < 0.05, Extended Data Table 2).
307 DMRs in voice-affecting genes are significantly more likely to be correlated with expression
308 compared to other DMRs (2.05x, $P = 6.65 \times 10^{-4}$, hypergeometric test). Particularly noteworthy
309 is *NFIX*, one of the most derived genes in AMHs (ranked 5th among DMGs affecting the
310 skeleton, Fig. 3a,b). *NFIX* contains two DMRs (#24 and #167, Fig. 5a), and in both, methylation
311 levels are tightly linked with expression (correlation of 81.7% and 73.8%, FDR = 3.5×10^{-6} and
312 8.6×10^{-5}, respectively, Fig. 5b). In fact, *NFIX* is one of the top ten DMGs with the most
313 significant correlation between methylation and expression in human. The association between
314 *NFIX* methylation and expression was also shown previously across several mouse tissues[33,34].
315 To further examine this, we investigated a dataset of DNMT3A-induced methylation of human
316 MCF-7 cells. Forced induction of methylation in this study was sufficient to repress *NFIX*
317 expression by over 50%, placing *NFIX* as one of the genes whose expression is most affected by
318 hypermethylation[35] (ranked in the 98th percentile, FDR = 1.28×10^{-6}). We further validated the
319 hypermethylation of *NFIX* across the skeleton by comparing four human cranial samples to four
320 chimpanzee cranial samples through bisulfite-PCR ($P = 0.01$, Extended Data Fig. 3, Extended
321 Data Table 1, see Methods). Together, these findings suggest that the observed hypermethylation

322 of *NFIX* in AMHs reflects down-regulation that emerged along the AMH lineage. Indeed, we
323 found that *NFIX*, as well as *SOX9, ACAN*, *COL2A1*, and *XYLT1* are hypermethylated in human
324 femora compared to baboon[36] ($P = 1.4 \times 10^{-5}$ and $P = 8.1 \times 10^{-9}$, compared to baboon femora
325 bone and cartilage, respectively, *t*-test). Also, all five genes show significantly reduced
326 expression in humans compared to mice (Fig. 5c). Taken together, these observations suggest
327 that DNA methylation is a primary mechanism in the regulation of *NFIX*, and serves as a good
328 proxy for its expression. Interestingly, NFI proteins were shown to bind the upstream enhancers
329 of *SOX9* [[37]], hence suggesting a possible mechanism to the simultaneous changes in the five top
330 genes we report.

331 Discussion

332 We have shown here that genes affecting vocal and facial anatomy went through extensive
333 methylation changes in recent AMH evolution, after the split from Neanderthals and Denisovans.
334 The extensive methylation changes are manifested both in the number of divergent genes and in
335 the extent of changes within each gene. Notably, the DMRs we report capture substantial
336 methylation changes (over 50% between at least one pair of human groups), span thousands or
337 tens of thousands of bases, and cover promoters and enhancers. Many of these methylation
338 changes are tightly linked with changes in expression. We particularly focused on changes in the
339 regulation of the five most derived skeletal genes on the AMH lineage: *SOX9*, *ACAN*, *COL2A1*,
340 *XYLT1*, and *NFIX*, whose downregulation was shown to underlie a retracted face, as well as
341 changes to the structure of the larynx[20,29,38–41]. The results we report, which are based on ancient
342 DNA methylation patterns, provide novel means to analyze the genetic mechanisms that underlie
343 the evolution of the human face and vocal tract.

344 Humans are distinguished from other apes in their unique capability to communicate through
345 speech. This capacity is attributed not only to neural changes, but also to structural alterations to
346 the vocal tract[42]. The relative roles of anatomy vs. cognition in our speech skills are still
347 debated[43], and some propose that even with a human brain, other apes could not reach the human
348 level of articulation and phonetic range[42,44]. Phonetic range is determined by the different
349 configurations that the vocal tract can produce. Modern humans have a 1:1 proportion between
350 the horizontal and vertical dimensions of the vocal tract, which develops mainly in post-infant
351 years[45] and is unique among primates (Fig. 6a)[42]. Although it is still debated whether this
352 configuration is a prerequisite for speech[43], it was nonetheless suggested to be optimal for
353 speech[42,46]. The 1:1 proportion was reached through retraction of the human face, together with
354 the descent of the larynx, pulling the tongue with it, and suggesting that the two process are
355 tightly linked[47,48]. In this regard, the fact that the top five skeletal DMGs regulate both facial
356 protrusion and the anatomy of the larynx suggests that these two processes might have been
357 linked, though the interaction between the two is still to be determined, as their exact
358 developmental pathways are beyond the scope of the current study. For an in-depth review of the
359 anatomy of vocalization and speech, see [42].
360 A longstanding question is whether Neanderthals and AMHs share similar vocal anatomy[49,50].
361 Attempts to answer this question based on morphological differences have proven hard, as the
362 larynx is mostly composed of soft tissues (e.g., cartilage), which do not survive long after death.
363 The only remnant from the Neanderthal laryngeal region is the hyoid bone, which is detached
364 from the rest of the skull[50]. Based on this single bone, or on computer simulations and tentative
365 vocal tract reconstructions, it is difficult to characterize the full anatomy of the Neanderthal
366 vocal apparatus, and opinions remain split as to whether it was similar to that of AMHs[49,50].

367 Most skeletal disease phenotypes that result from *NFIX* dysfunction are craniofacial, as *NFIX*
368 influences the balance between lower and upper projection of the face[51]. In addition, mutations in
369 *NFIX* were shown to impair speech capabilities[41,52]. The exact mechanism is still unknown, but is
370 thought to occur partly through skeletal alterations to the larynx[41]. To investigate if changes in
371 *NFIX* expression could explain morphological changes in the AMH face and larynx, we
372 examined its clinical skeletal phenotypes. Mutations in *NFIX* were shown to cause the Marshall-
373 Smith and Malan syndromes, whose phenotypes include various skeletal alterations such as
374 hypoplasia of the midface, retracted lower jaw, and depressed nasal bridge[51]. In many patients,
375 the phenotypic alterations are driven by heterozygous loss-of-function mutations that cause
376 haploinsufficiency. This shows that reduced activity of *NFIX*, even if partial, results in skeletal
377 alterations[51]. Because *NFIX* is inferred to have been down-regulated in AMHs compared to
378 archaic humans, we hypothesized that similar phenotypes to the ones that are driven by *NFIX*
379 loss-of-function may also exist between modern and archaic humans. For example, because
380 reduced activity of *NFIX* results in a more retracted face, we hypothesized that AMHs would
381 present a more retracted face compared to archaic humans. We therefore examined the
382 phenotypes of the Marshall-Smith and Malan syndromes and found that not only do most of
383 these phenotypes exist between Neanderthals and modern humans, but their direction matches
384 the direction expected from NFIX down-regulation along the AMH lineage (18 out of the 22
385 Marshall-Smith phenotypes, and 8 out of the 9 Malan phenotypes, $P = 6.0 \times 10^{-4}$, binomial test).
386 In other words, from the Neanderthal, where *NFIX* activity is expected to be highest, through
387 healthy AMHs, to individuals with *NFIX* haploinsufficiency, phenotypic manifestation matches
388 the level of *NFIX* activity (Fig. 6b, Extended Data Table 8).

389 Notably, many cases of laryngeal malformations in the Marshall-Smith syndrome have been
390 reported. Some of the patients exhibit positional changes to the larynx, changes in its width, and,
391 more rarely, structural alterations to the arytenoid cartilage – the anchor point of the vocal folds,
392 which controls their movement[53]. In fact, these laryngeal and facial changes are thought to
393 underlie some of the limited speech capabilities observed in various patients[41]. This raises the
394 possibility that *NFIX* down-regulation in AMHs might have driven phenotypic changes in the
395 larynx too.
396 *SOX9*, *ACAN*, *COL2A1*, *XYLT1*, and *NFIX* are active in early stages of osteochondrogenesis,
397 making the observation of differential methylation in mature bones puzzling at first glance. This
398 could potentially be explained by two factors: (i) The methylome stabilizes as development
399 progresses and remains largely unchanged from late development through adulthood. Thus, adult
400 methylation states often reflect earlier development, and DMRs in adult stages often reflect
401 DMRs in earlier activity levels[3,17,54]. Therefore, these DMRs might reflect early methylation
402 changes in mesenchymal progenitors that are carried over to later stages of osteogenesis. Indeed,
403 the methylation patterns of *NFIX*, *SOX9*, *ACAN*, and *COL2A1* were shown to be established in
404 early stages of human development and remain stable throughout differentiation from
405 mesenchymal stem cells to mature osteocytes[55]. It is further supported by the observation that
406 osteoblasts and chondrocytes show almost identical methylation levels in these DMRs, and are
407 all as hypermethylated as the adult bone methylation levels we report[56]. We have reconfirmed
408 this result by measuring methylation in these DMGs in primary human chondrocytes. Finally, we
409 show that the upstream mesenchymal enhancer of *SOX9*[[23]] is differentially methylated in AMHs
410 (Fig. 4b). (ii) Although expression levels of *SOX9*, *ACAN*, and *COL2A1* gradually decrease with
411 skeletal maturation, these genes were shown to remain active in later developmental stages in the

412 larynx, vertebrae, limbs, and jaws, including in their osteoblasts[21,57]. Interestingly, these are also
413 the organs that are most affected by mutations in these genes, implying that their late stages of
414 activity might still play important roles in morphological patterning[20,38–40]. It was also shown that
415 facial growth patterns, which shape facial prognathism, differ between archaic and modern
416 humans not only during early development, but also as late as adolescence[58]. Moreover, the main
417 differences between human and chimp vocal tracts are established during post-infant years[45].
418 Although the DMRs we report most likely exist throughout the skeleton, including the larynx,
419 the evidence we present for the cranium is more direct, as the patterns are observed in modern
420 human and chimpanzee crania. Importantly, it has been suggested that the 1:1 vocal
421 conformation could have been entirely driven by cranial, rather than laryngeal, alterations[48].
422 Once archaic human cranial samples are sequenced, these observations could be more directly
423 tested.
424 The results we presented open a window to study the evolution of the human vocal tract and face
425 from genetic and epigenetic perspectives. Our data suggest shared genetic mechanisms that
426 shaped these anatomical regions and point to evolutionary events that separate AMHs from the
427 Neanderthal and Denisovan. The mechanisms leading to such extensive regulatory shifts, as well
428 as if and to what extent these evolutionary changes affected vocalization and speech capabilities
429 are still to be determined.

430 # References

431 1. Prüfer, K. *et al.* The complete genome sequence of a Neanderthal from the Altai Mountains.
432 *Nature* **505**, 43–9 (2014).
433 2. King, M. C. & Wilson, A. C. Evolution at two levels in humans and chimpanzees. *Science* **188**,
434 107–116 (1975).
435 3. Hernando-Herraez, I., Garcia-Perez, R., Sharp, A. J. & Marques-Bonet, T. DNA Methylation:
436 Insights into Human Evolution. *PLoS Genetics* **11**, e1005661 (2015).
437 4. Gokhman, D. *et al.* Reconstructing the DNA methylation maps of the Neandertal and the
438 Denisovan. *Science* **344**, 523–527 (2014).
439 5. Prüfer, K. *et al.* A high-coverage Neandertal genome from Vindija Cave in Croatia. *Science (80-.*
440 *).* **358**, 655–658 (2017).
441 6. Fu, Q. *et al.* Genome sequence of a 45,000-year-old modern human from western Siberia. *Nature*
442 **514**, 445–9 (2014).
443 7. Lazaridis, I. *et al.* Ancient human genomes suggest three ancestral populations for present-day
444 Europeans. *Nature* **513**, 409–413 (2014).
445 8. Olalde, I. *et al.* Derived immune and ancestral pigmentation alleles in a 7,000-year-old Mesolithic
446 European. *Nature* **507**, 225–228 (2014).
447 9. Mathieson, I. *et al.* Genome-wide patterns of selection in 230 ancient Eurasians. *Nature* **528**, 499–
448 503 (2015).
449 10. Gokhman, D., Malul, A. & Carmel, L. Inferring Past Environments from Ancient Epigenomes.
450 *Mol. Biol. Evol.* **34**, 2429–2438 (2017).
451 11. Gokhman, D. *et al.* Gene ORGANizer: Linking genes to the organs they affect. *Nucleic Acids Res.*
452 **45**, W138–W145 (2017).
453 12. Aiello, L. & Dean, C. *An Introduction to Human Evolutionary Anatomy*. (Elsevier, 2002).
454 13. Prescott, S. L. *et al.* Enhancer Divergence and cis-Regulatory Evolution in the Human and Chimp

455 Neural Crest. *Cell* **163**, 68–84 (2015).

456 14. Wilderman, A., VanOudenhove, J., Kron, J., Noonan, J. P. & Cotney, J. High-Resolution
457 Epigenomic Atlas of Human Embryonic Craniofacial Development. *Cell Rep.* **23**, 1581–1597
458 (2018).

459 15. MacArthur, J. *et al.* The new NHGRI-EBI Catalog of published genome-wide association studies
460 (GWAS Catalog). *Nucleic Acids Res.* **45**, D896–D901 (2017).

461 16. Hernando-Herraez, I. *et al.* The interplay between DNA methylation and sequence divergence in
462 recent human evolution. *Nucleic Acids Res* **43**, 8204–8214 (2015).

463 17. Schultz, M. D. *et al.* Human body epigenome maps reveal noncanonical DNA methylation
464 variation. *Nature* **523**, 212–6 (2015).

465 18. Peyrégne, S., Boyle, M. J., Dannemann, M. & Prüfer, K. Detecting ancient positive selection in
466 humans using extended lineage sorting. *Genome Res.* **27**, 1563–1572 (2017).

467 19. Köhler, S. *et al.* The Human Phenotype Ontology project: Linking molecular biology and disease
468 through phenotype data. *Nucleic Acids Res.* **42**, (2014).

469 20. Lee, Y. H. & Saint-Jeannet, J. P. Sox9 function in craniofacial development and disease. *Genesis*
470 **49**, 200–208 (2011).

471 21. Ng, L. J. *et al.* Sox9 binds DNA, activates transcription, and coexpresses with type II collagen
472 during chondrogenesis in the mouse. *Dev. Biol.* **183**, 108–121 (1997).

473 22. Claes, P. *et al.* Genome-wide mapping of global-to-local genetic effects on human facial shape.
474 *Nat. Genet.* **50**, 414–423 (2018).

475 23. Yao, B. *et al.* The SOX9 upstream region prone to chromosomal aberrations causing campomelic
476 dysplasia contains multiple cartilage enhancers. *Nucleic Acids Res.* **43**, 5394–5408 (2015).

477 24. Kim, K. Il, Park, Y. S. & Im, G. Il. Changes in the epigenetic status of the SOX-9 promoter in
478 human osteoarthritic cartilage. *J. Bone Miner. Res.* **28**, 1050–1060 (2013).

479 25. Claes, P. *et al.* Modeling 3D Facial Shape from DNA. *PLoS Genet.* **10**, e1004224 (2014).

480 26. Cheng, P. F. *et al.* Methylation-dependent SOX9 expression mediates invasion in human

481 melanoma cells and is a negative prognostic factor in advanced melanoma. *Genome Biol.* **16**, 42
482 (2015).
483 27. Huang, C.-Z. *et al.* Sox9 transcriptionally regulates Wnt signaling in intestinal epithelial stem cells
484 in hypomethylated crypts in the diabetic state. *Stem Cell Res. Ther.* **8**, 60 (2017).
485 28. Pamnani, M., Sinha, P., Singh, A., Nara, S. & Sachan, M. Methylation of the Sox9 and Oct4
486 promoters and its correlation with gene expression during testicular development in the laboratory
487 mouse. *Genet. Mol. Biol.* **39**, 452–458 (2016).
488 29. Hall, B. D. Lethality in Desbuquois dysplasia: Three new cases. *Pediatr. Radiol.* **31**, 43–47
489 (2001).
490 30. LaCroix, A. J. *et al.* GGC Repeat Expansion and Exon 1 Methylation of XYLT1 Is a Common
491 Pathogenic Variant in Baratela-Scott Syndrome. *Am. J. Hum. Genet.* (2018).
492 doi:https://doi.org/10.1016/j.ajhg.2018.11.005
493 31. Ohba, S., He, X., Hojo, H. & McMahon, A. P. Distinct Transcriptional Programs Underlie Sox9
494 Regulation of the Mammalian Chondrocyte. *Cell Rep.* **12**, 229–243 (2015).
495 32. Roadmap Epigenomics Consortium *et al.* Integrative analysis of 111 reference human epigenomes.
496 *Nature* **518**, 317–329 (2015).
497 33. Carrió, E. *et al.* Deconstruction of DNA methylation patterns during myogenesis reveals specific
498 epigenetic events in the establishment of the skeletal muscle lineage. *Stem Cells* **33**, 2025–2036
499 (2015).
500 34. Maunakea, A. K. *et al.* Conserved role of intragenic DNA methylation in regulating alternative
501 promoters. *Nature* **466**, 253–7 (2010).
502 35. Ford, E. E. *et al.* Frequent lack of repressive capacity of promoter DNA methylation identified
503 through genome-wide epigenomic manipulation. *bioRxiv* (2018).
504 doi:https://doi.org/10.1101/170506
505 36. Housman, G., Havill, L. M., Quillen, E. E., Comuzzie, A. G. & Stone, A. C. Assessment of DNA
506 Methylation Patterns in the Bone and Cartilage of a Nonhuman Primate Model of Osteoarthritis.

Cartilage (2018). doi:10.1177/1947603518759173

37. Pjanic, M. *et al.* Nuclear Factor I genomic binding associates with chromatin boundaries. *BMC Genomics* **14**, 99 (2013).

38. Tompson, S. W. *et al.* A Recessive Skeletal Dysplasia, SEMD Aggrecan Type, Results from a Missense Mutation Affecting the C-Type Lectin Domain of Aggrecan. *Am. J. Hum. Genet.* **84**, 72–79 (2009).

39. Frenzel, K., Amann, G. & Lubec, B. Deficiency of laryngeal collagen type II in an infant with respiratory problems. *Arch. Dis. Child.* **78**, 557–9 (1998).

40. Hoornaert, K. P. *et al.* Stickler syndrome caused by COL2A1 mutations: genotype–phenotype correlation in a series of 100 patients. *Eur J Hum Genet.* **18**, 872–880 (2010).

41. Shaw, A. C. *et al.* Phenotype and natural history in Marshall-Smith syndrome. *Am. J. Med. Genet. Part A* **152**, 2714–2726 (2010).

42. Lieberman, P. The Evolution of Human Speech: Its Anatomical and Neural Bases. *Curr. Anthropol.* **48**, 39–66 (2007).

43. Fitch, W. T., de Boer, B., Mathur, N. & A. Ghazanfar, A. Response to Lieberman on "Monkey vocal tracts are speech-ready". *Sci. Adv.* **3**, (2017).

44. Lieberman, P. Comment on "Monkey vocal tracts are speech-ready". *Sci. Adv.* **3**, (2017).

45. Nishimura, T. Developmental changes in the shape of the supralaryngeal vocal tract in Chimpanzees. *Am. J. Phys. Anthropol.* (2005). doi:10.1002/ajpa.20112

46. De Boer, B. Modelling vocal anatomy's significant effect on speech. *J. Evol. Psychol.* **8**, 351–366 (2010).

47. Lieberman, D. E. *The Evolution of the Human Head*. (Harvard University Press, 2011).

48. Nishimura, T., Mikami, A., Suzuki, J. & Matsuzawa, T. Descent of the hyoid in chimpanzees: evolution of face flattening and speech. *J. Hum. Evol.* **51**, 244–254 (2006).

49. Fitch, W. T. The evolution of speech: A comparative review. *Trends in Cognitive Sciences* **4**, 258–267 (2000).

533 50. Steele, J., Clegg, M. & Martelli, S. Comparative morphology of the hominin and african ape hyoid
534 bone, a possible marker of the evolution of speech. *Hum Biol* **85**, 639–672 (2013).
535 51. Malan, V. *et al.* Distinct effects of allelic NFIX mutations on nonsense-mediated mRNA decay
536 engender either a sotos-like or a Marshall-Smith Syndrome. *Am. J. Hum. Genet.* **87**, 189–198
537 (2010).
538 52. Van Balkom, I. D. C. *et al.* Development and behaviour in Marshall-Smith syndrome: An
539 exploratory study of cognition, phenotype and autism. *J. Intellect. Disabil. Res.* (2011).
540 doi:10.1111/j.1365-2788.2011.01451.x
541 53. Cullen, A., Clarke, T. A. & O'Dwyer, T. P. The Marshall-Smith syndrome: a review of the
542 laryngeal complications. *Eur J Pediatr* **156**, 463–464 (1997).
543 54. Ziller, M. J. *et al.* Charting a dynamic DNA methylation landscape of the human genome. *Nature*
544 **500**, 477–481 (2013).
545 55. Håkelien, A. M. *et al.* The regulatory landscape of osteogenic differentiation. *Stem Cells* **32**,
546 2780–2793 (2014).
547 56. Bernstein, B. E. *et al.* An integrated encyclopedia of DNA elements in the human genome. *Nature*
548 **489**, 57–74 (2012).
549 57. Moriarity, B. S. *et al.* A Sleeping Beauty forward genetic screen identifies new genes and
550 pathways driving osteosarcoma development and metastasis. *Nat. Genet.* **47**, 615–24 (2015).
551 58. Lacruz, R. S. *et al.* Ontogeny of the maxilla in Neanderthals and their ancestors. *Nat. Commun.* **6**,
552 8996 (2015).
553 59. Horvath, S. *et al.* The cerebellum ages slowly according to the epigenetic clock. *Aging (Albany.*
554 *NY).* **7**, 294–306 (2015).
555 60. Kulis, M. *et al.* Whole-genome fingerprint of the DNA methylome during human B cell
556 differentiation. *Nat. Genet.* **47**, 746–756 (2015).
557 61. Marco-Sola, S., Sammeth, M., Guigó, R. & Ribeca, P. The GEM mapper: fast, accurate and
558 versatile alignment by filtration. *Nat. Methods* **9**, 1185–1188 (2012).

559 62. Hansen, K. D., Langmead, B. & Irizarry, R. A. BSmooth: from whole genome bisulfite sequencing
560 reads to differentially methylated regions. *Genome Biol.* (2012). doi:10.1186/gb-2012-13-10-R83
561 63. Dabney, J. *et al.* Complete mitochondrial genome sequence of a Middle Pleistocene cave bear
562 reconstructed from ultrashort DNA fragments. *Proc. Natl. Acad. Sci. U. S. A.* **110**, 15758–63
563 (2013).
564 64. Rohland, N. & Hofreiter, M. Ancient DNA extraction from bones and teeth. *Nat. Protoc.* **2**, 1756–
565 1762 (2007).
566 65. Boyle, P. *et al.* Gel-free multiplexed reduced representation bisulfite sequencing for large-scale
567 DNA methylation profiling. *Genome Biol.* **13**, R92 (2012).
568 66. Barnett, R. & Larson, G. A phenol-chloroform protocol for extracting DNA from ancient samples.
569 *Methods Mol. Biol.* **840**, 13–19 (2012).
570 67. Fortin, J.-P., Triche, T. & Hansen, K. Preprocessing, normalization and integration of the Illumina
571 HumanMethylationEPIC array. *bioRxiv* 065490 (2016). doi:10.1101/065490
572 68. Hernando-Herraez, I. *et al.* Dynamics of DNA Methylation in Recent Human and Great Ape
573 Evolution. *PLOS Genet* **9**, e1003763 (2013).
574 69. Emonet, E. G. & Kullmer, O. Variability in premolar and molar root number in a modern
575 population of pan troglodytes verus. *Anat. Rec.* **297**, 1927–1934 (2014).
576 70. Sirak, K. A. *et al.* A minimally-invasive method for sampling human petrous bones from the
577 cranial base for ancient DNA analysis. *Biotechniques* **62**, 283–289 (2017).
578 71. Haak, W. *et al.* Massive migration from the steppe was a source for Indo-European languages in
579 Europe. *Nature* **522**, 207–211 (2015).
580 72. Gokhman, D., Meshorer, E. & Carmel, L. Epigenetics: It's Getting Old. Past Meets Future in
581 Paleoepigenetics. *Trends Ecol. Evol.* **31**, 290–300 (2016).
582 73. Hanghøj, K. *et al.* Fast, Accurate and Automatic Ancient Nucleosome and Methylation Maps with
583 epiPALEOMIX. *Mol. Biol. Evol.* **33**, 3284–3298 (2016).
584 74. Huang, D. W., Lempicki, R. a & Sherman, B. T. Systematic and integrative analysis of large gene

585 lists using DAVID bioinformatics resources. *Nat. Protoc.* **4**, 44–57 (2009).
586 75. Blasi, D. E. *et al.* Human sound systems are shaped by post-Neolithic changes in bite
587 configuration. *Science (80-.).* (2019). doi:10.1126/science.aav3218
588 76. Guo, M. *et al.* Epigenetic profiling of growth plate chondrocytes sheds insight into regulatory
589 genetic variation influencing height. *Elife* **6**, (2017).
590 77. Bagheri-Fam, S. *et al.* Long-range upstream and downstream enhancers control distinct subsets of
591 the complex spatiotemporal Sox9 expression pattern. *Dev. Biol.* **291**, 382–397 (2006).
592 78. Sekido, R. & Lovell-Badge, R. Sex determination involves synergistic action of SRY and SF1 on a
593 specific Sox9 enhancer. *Nature* **453**, 930–934 (2008).
594 79. Varanasi, S. S. *et al.* Skeletal site-related variation in human trabecular bone transcriptome and
595 signaling. *PLoS One* **5**, e10692 (2010).
596 80. Martynoga, B. *et al.* Epigenomic enhancer annotation reveals a key role for NFIX in neural stem
597 cell quiescence. *Genes Dev.* **27**, 1769–1786 (2013).
598 81. Waki, H. *et al.* Global mapping of cell type-specific open chromatin by FAIRE-seq reveals the
599 regulatory role of the NFI family in adipocyte differentiation. *PLoS Genet.* **7**, e1002311 (2011).
600

601 ## Acknowledgements

602 We would like to thank Sagiv Shifman, Yoel Rak, Rodrigo Lacruz, Erella Hovers, Anna Belfer-
603 Cohen, Achinoam Blau, Iain Mathieson, Philip Lieberman, Daniel Lieberman, and Terry
604 Capellini for their useful advice, Svante Pääbo, Janet Kelso, Kay Prüfer, Johannes Krause, and
605 Anne Pusey for providing data, Sjaak Kaandorp and Christine Kaandorp-Huber from Safari park
606 Beekse Bergen in Netherlands for their cooperation in animal conservation and use for research,
607 and Maayan Harel for illustrations. D.G. is supported by the Clore Israel Foundation. TMB is
608 supported by BFU2017-86471-P (MINECO/FEDER, UE), U01 MH106874 grant, Howard
609 Hughes International Early Career, Obra Social "La Caixa" and Secretaria d'Universitats i
610 Recerca and CERCA Programme del Departament d'Economia i Coneixement de la Generalitat
611 de Catalunya. D.R. is an Investigator of the Howard Hughes Medical Institute and is also
612 supported by an Allen Discovery Center for the Study of Human Brain Evolution funded the
613 Paul G. Allen Family Foundation. C.L.-F. is supported by FEDER and BFU2015-64699-P grant
614 from the Spanish government. R.P. was supported by ERC starting grant ADNABIOARC
615 (263441). R.M.G. and J.M.O are supported by NYSTEM contract C030133. Funding for the
616 collection and processing of the 850K chimp data was provided by the Leakey Foundation
617 Research Grant for Doctoral Students, Wenner-Gren Foundation Dissertation Fieldwork Grant
618 (Gr. 9310), James F. Nacey Fellowship from the Nacey Maggioncalda Foundation, International
619 Primatological Society Research Grant, Sigma Xi Grant-in-Aid of Research, Center for
620 Evolution and Medicine Venture Fund (ASU), Graduate Research and Support Program Grant
621 (GPSA, ASU), and Graduate Student Research Grant (SHESC, ASU) to G.H. Collection of the
622 chimpanzee bone from Tanzania was funded by the Jane Goodall Institute, and grants from the

US National Institutes of Health (AI 058715) and National Science Foundation (IOS-1052693), and facilitated by Elizabeth Lonsdorf and Beatrice Hahn.

Author Contributions

D.G. planned and conducted analyses. L.C. supervised the computational and experimental work. E.M. supervised experiments. L.A.T, B.Y, D.G. and L.C. conceived statistical analyses. D.G., L.C, and E.M. wrote the manuscript. All other authors contributed to the production of data and wrote their respective parts of the manuscript.

Tables and Figures

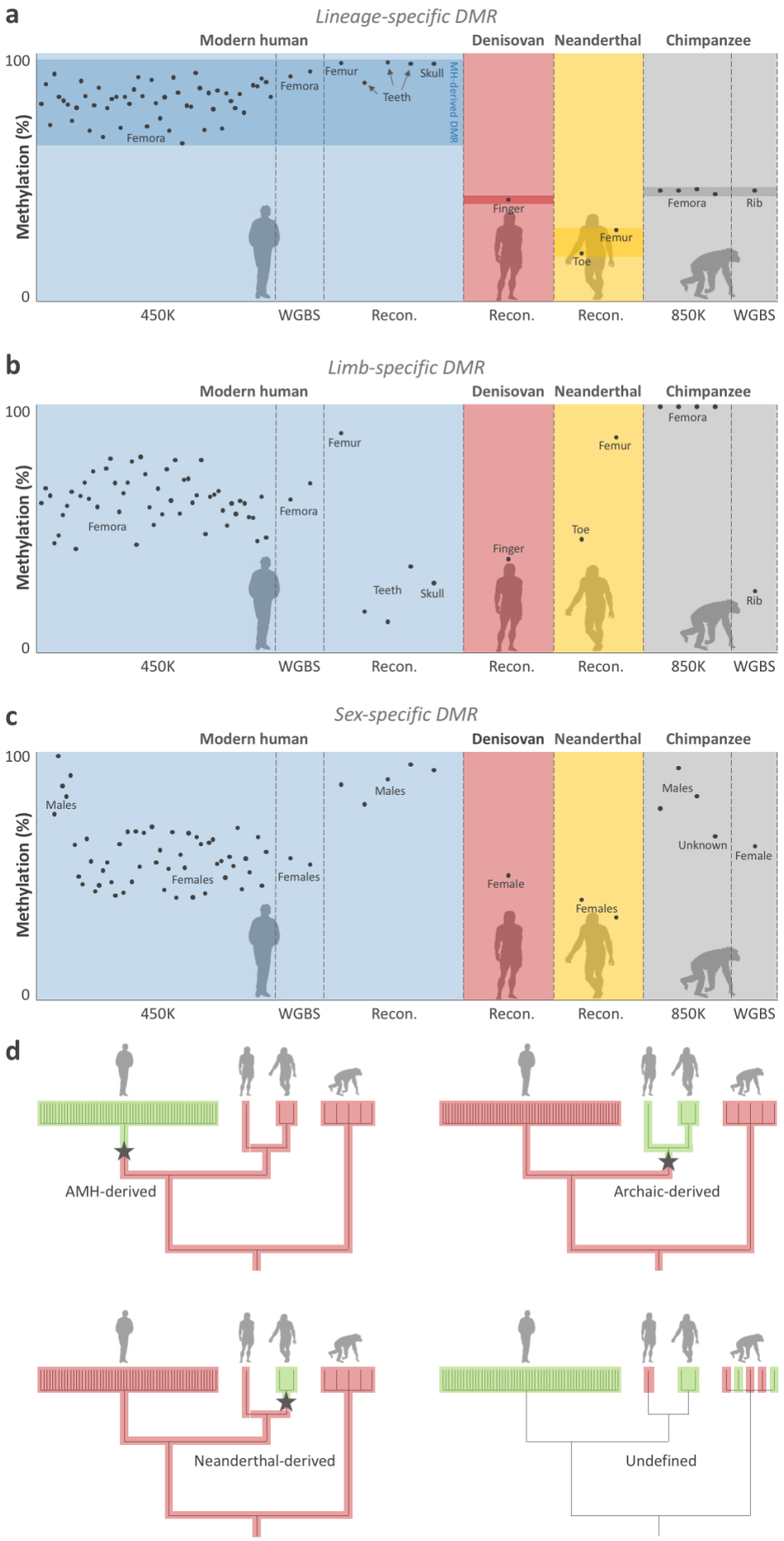
a
Lineage-specific DMR
Modern human
Denisovan
Neanderthal
Chimpanzee
Methylation (%)
100
0
Femora
Femur
Skull
Teeth
MH-derived DMR
Finger
Toe
Rib
450K
WGBS
Recon.
850K
b
Limb-specific DMR
c
Sex-specific DMR
Males
Females
Female
Unknown
d
AMH-derived
Archaic-derived
Neanderthal-derived
Undefined

632 **Figure 1. Variability filtering and lineage assignment. a.** Methylation levels across AMH,
633 Denisovan, Neanderthal, and chimpanzee samples in DMR#278 (chr4:38,014,896-38,016,197).
634 This is an example of a lineage-specific DMR, defined as a locus in which all samples of a group
635 are found outside the range of methylation in the other groups. Chimpanzee samples were used
636 during the following step of lineage assignment. **b.** A putative limb-specific DMR
637 (chr3:14,339,371-14,339,823) which was removed from the analysis, as it does not comply with
638 our definition of lineage-specific DMRs. Femur, toe, and finger samples are hypermethylated
639 compared to other skeletal elements. Toe and finger are found at the bottom range of limb
640 samples, suggesting some variation in this locus within limb samples too. **c.** A putative sex-
641 specific DMR (chr3:72,394,336-72,396,901) which was removed from the analysis. Males are
642 hypermethylated compared to females. **d.** Lineage assignment using chimpanzee samples. Each
643 bar at the tree leaves represents a sample. Methylation levels are marked with red and green,
644 representing methylated and unmethylated samples, respectively. Only DMRs that passed the
645 previous variability filtering steps were analyzed. The lineage where the methylation change has
646 likely occurred (by parsimony) is marked by a star. Branch lengths are not scaled.

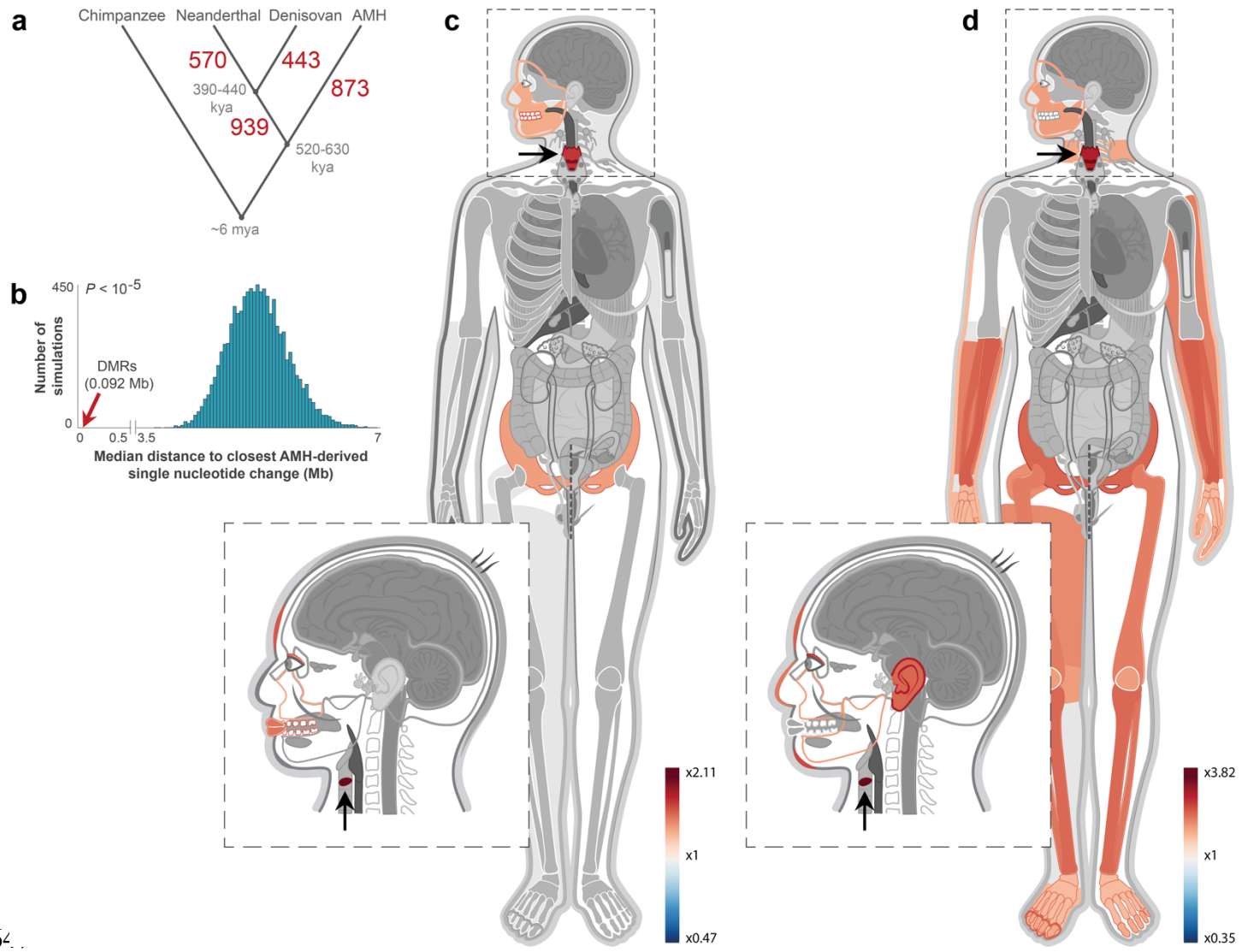

Figure 2. Genes affecting voice and face are the most over-represented within AMH-derived DMRs. a. The number of DMRs that emerged along each of the human branches. Divergence times are in thousands of years ago (kya). **b**. Distribution of median distances (turquoise) of DMRs to randomized single nucleotide changes that separate AMHs from archaic humans and chimpanzees. Genomic positions of single nucleotide changes were allocated at random. This was repeated 10,000 times. Red arrow marks the observed distance of DMRs, showing that they tend to be significantly closer to AMH-derived single nucleotide changes than expected by chance. This suggests that some of these sequence changes might have driven the

656 changes in methylation. **c.** A heat map representing the level of enrichment of each anatomical
657 part within the AMH-derived DMRs. Only body parts that are significantly enriched (FDR <
658 0.05) are colored. Three skeletal parts are significantly over-represented: the face, pelvis, and
659 larynx (voice box, marked with arrows). **d.** Enrichment levels of anatomical parts within the
660 most significant (top quartile, Q statistic) AMH-derived DMRs, showing a more pronounced
661 enrichment of genes affecting vocal and facial anatomy.

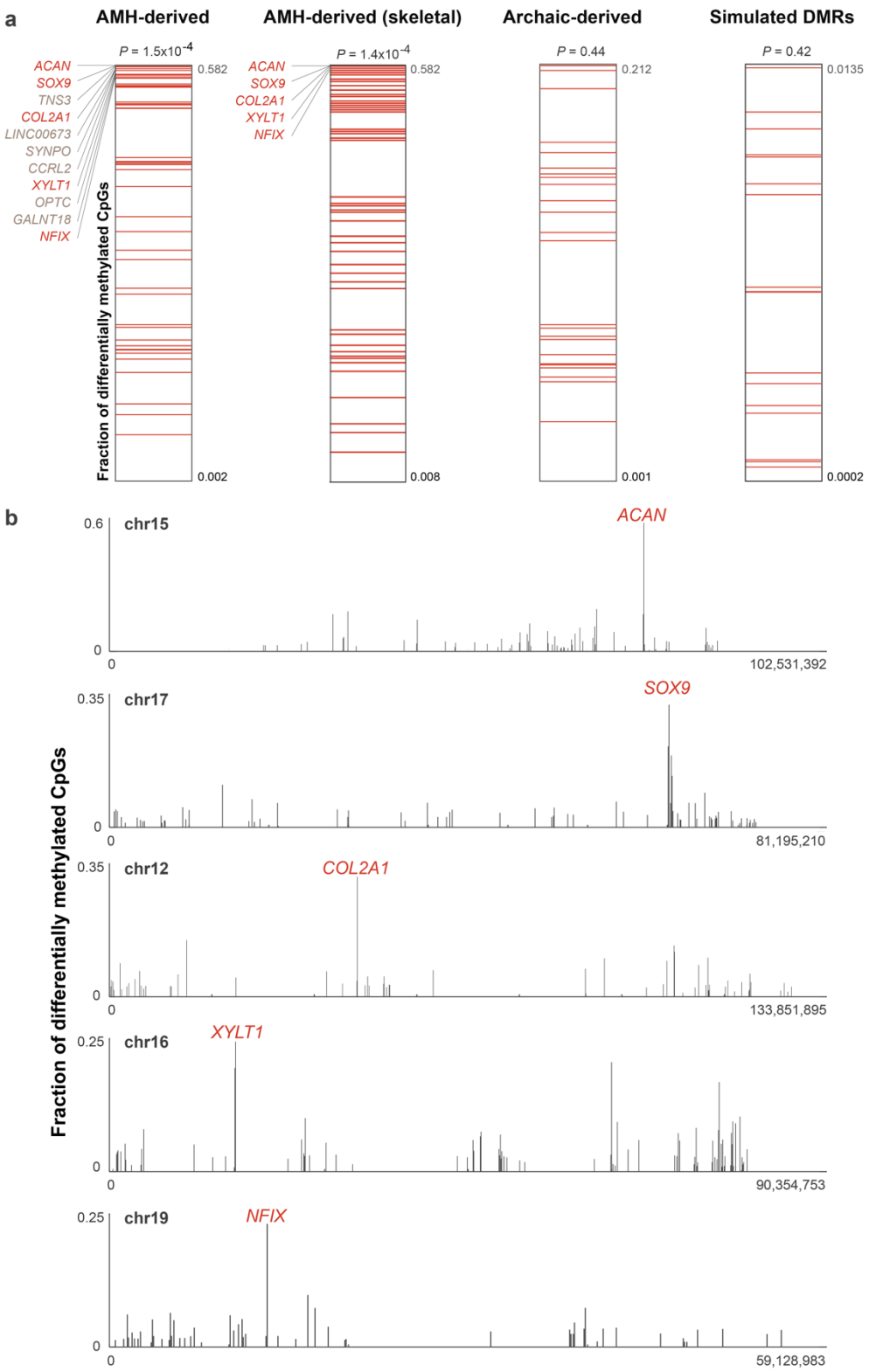

Figure 3. The extent of differential methylation is highest among genes affecting the voice. **a.** Within each lineage, the fraction of differentially methylated CpGs was computed as the

665 number of derived CpGs per 100 kb centered around the middle of each DMR. Genes were
666 ranked according to the fraction of derived CpG positions within them. Genes affecting the voice
667 are marked with red lines. AMH-derived DMRs in voice-affecting genes tend to be ranked
668 significantly higher. Although these genes comprise less than 2% of the genome, three of the top
669 five AMH-derived DMRs, and all top five skeleton-related AMH-derived DMRs are in genes
670 that affect the voice. In archaic-derived DMRs and in simulated DMRs, voice-affecting genes do
671 not show higher ranking compared to the rest of the DMGs. **b.** The fraction of differentially
672 methylated CpGs along the five chromosomes containing *ACAN*, *SOX9*, *COL2A1*, *XYLT1*, and
673 *NFIX*. In each of these chromosomes, the most extensive changes are found within these genes.
674 All five genes control facial projection and the development of the larynx.
675

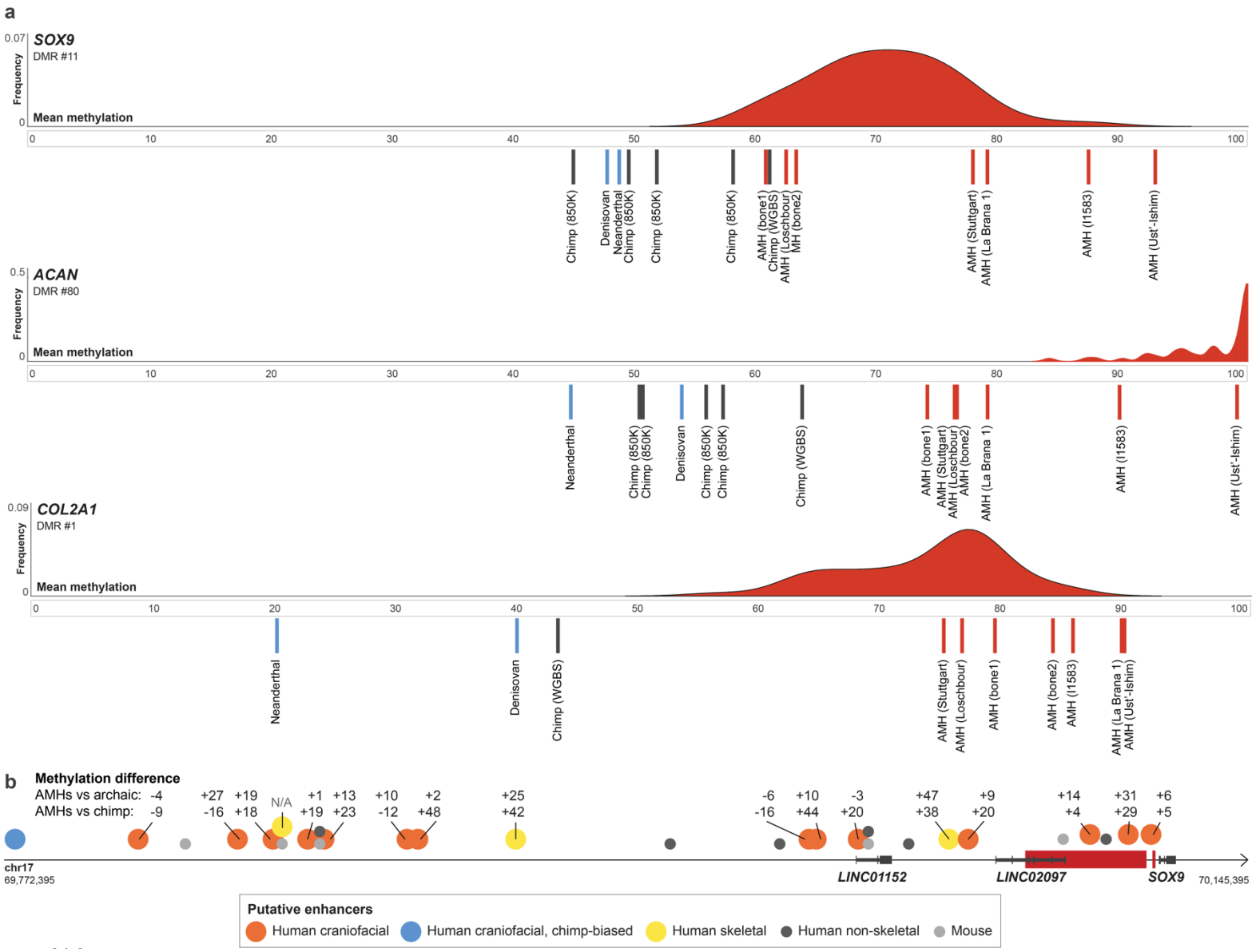

Figure 4. Hypermethylation of *SOX9*, *ACAN*, and *COL2A1* in AMHs. a. Methylation levels in the AMH-derived DMRs in *SOX9*, *ACAN*, and *COL2A1*. AMH samples are marked with red lines, archaic human samples are marked with blue lines and chimpanzee samples are marked with grey lines. The distribution of methylation across 52 AMH samples (450K methylation arrays) is presented in red. **b.** *SOX9* and its upstream regulatory elements. AMH-derived DMRs are marked with red rectangles. Previously identified putative enhancers are marked with circles. Numbers above skeletal enhancers show the difference in mean bone methylation between

684 AMHs and archaic humans (top) and between AMHs and chimpanzee (bottom). Across almost
685 all *SOX9* enhancers, AMHs are hypermethylated compared to archaic humans and the
686 chimpanzee.
687

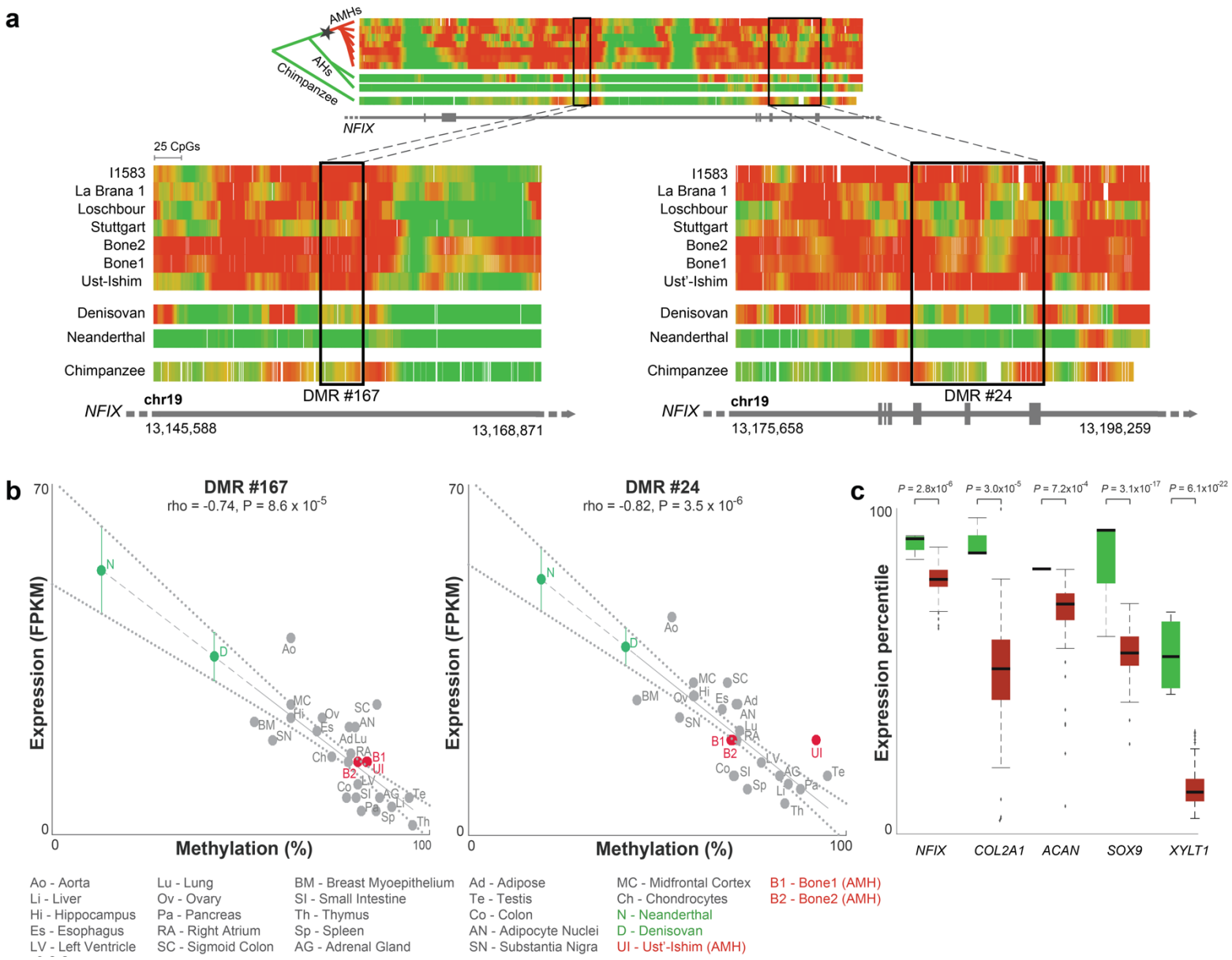

Figure 5. *NFIX* became down-regulated after the split from archaic humans. a. Methylation levels along *NFIX*, color-coded from green (unmethylated) to red (methylated). Methylation levels around the two AMH-derived DMRs (#24 and #167) are shown in the zoomed-in panels. These two DMRs represent the regions where the most significant methylation changes are observed, but hypermethylation of *NFIX* in AMHs can be seen throughout the entire gene body. Chimpanzee and present-day samples were smoothed using the same sliding window as in ancient samples to allow easier comparison. The inferred schematic regulatory evolution of

696 *NFIX* is shown using a phylogenetic tree to the left of the top panel. Star marks the shift in
697 methylation from unmethylated (green) to methylated (red). **b**. Methylation levels in DMRs #167
698 and #24 vs. expression levels of *NFIX* across 22 AMH tissues (grey). In both DMRs, higher
699 methylation is significantly associated with lower expression of *NFIX*. Ust'-Ishim, Bone1 and
700 Bone2 methylation levels (red) are plotted against mean NFIX expression across 13 osteoblast
701 lines. Neanderthal and Denisovan methylation levels (green) are plotted against the predicted
702 expression levels, based on the extrapolated regression line (dashed). Standard errors are marked
703 with dotted lines. The Neanderthal and Denisovan are expected to have higher *NFIX* expression
704 levels. **c.** Expression levels of *NFIX, COL2A1, ACAN, SOX9* and *XYLT1* in AMHs are reduced
705 compared to mice. Box plots present 89 human samples (red) and four mouse samples (green)
706 from appendicular bones (limbs and pelvis). Expression levels were converted to percentiles
707 based on the level of gene expression compared to the rest of the genome in each sample.

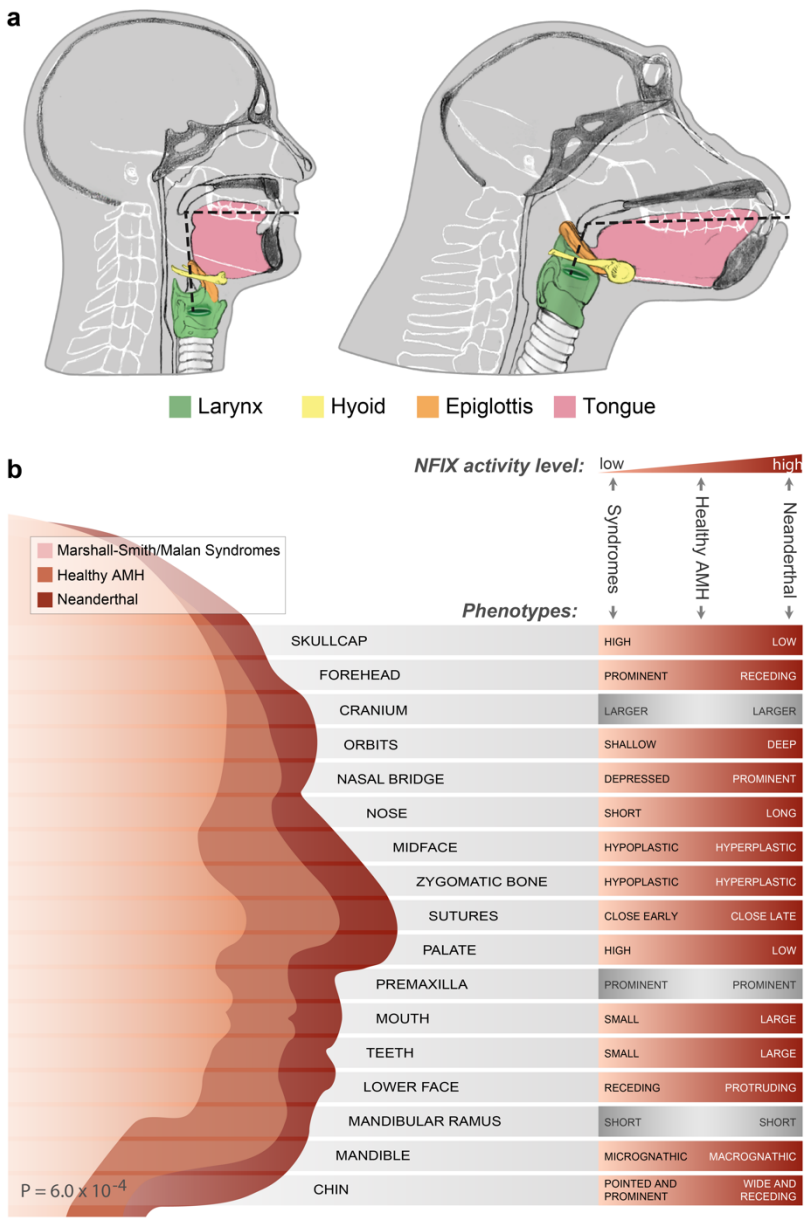

Figure 6. *NFIX* down-regulation may underlie modern human-derived traits. a. Vocal anatomy of chimpanzee and AMH. The vocal tract is the cavity from the lips to the larynx (marked by dashed lines). In AMHs, the flattening of the face together with the descent of the larynx led to approximately 1:1 proportions of the horizontal and vertical portions of the vocal tract. **b**. Craniofacial features of the Neanderthal, healthy AMH, and AMH with Marshall-Smith

714 or Malan syndromes. Each box shows a phenotype that occurs in the Marshall-Smith/Malan
715 syndromes (i.e., when *NFIX* is partially or completely inactive). The righthand side of each box
716 shows the observed phenotypes of individuals with the syndromes (left), healthy AMHs (middle)
717 and Neanderthals (right). In most phenotypes, the observed phenotypes match the expected
718 phenotypes based on *NFIX* expression.
719

720 # Methods

721 ## Skeletal Methylation Maps

722 Previously, our ability to identify differentially methylated regions (DMRs) that discriminate
723 between human groups was confined by three main factors: (i) We had a single DNA
724 methylation map from a present-day human bone, which was produced using a reduced
725 representation bisulfite sequencing (RRBS) protocol, which provides information for only ~10%
726 of CpG positions in the genome. Moreover, the fact that the archaic and present-day methylomes
727 were produced using different technologies – computational reconstruction versus RRBS –
728 potentially introduces a bias. (ii) The analyses included only one bone methylation map from
729 each of the human groups, which limited our ability to identify fixed differences between the
730 groups. Although dozens of maps from additional tissues in present-day humans were included
731 in the analyses, this narrowed the DMRs to represent only human-specific changes that are
732 invariable between tissues. (iii) The work did not include a great ape outgroup. Thus, when a
733 AMH-specific change was identified, it was impossible to determine whether it happened on the
734 AMH lineage, or in the ancestor of Neanderthals and Denisovans[4].
735 To overcome these obstacles, a major goal of the current study was to significantly extend the
736 span of our skeletal methylome collection, covering as many individuals, sexes, and bone types
737 as we could. This included the generation of many new samples, including the high-coverage
738 sequencing of additional ancient genomes, as listed below.

739 ### Present-day human bone DNA methylation maps

740 We generated full DNA methylation maps from two femur head bones from present-day humans
741 using whole-genome bisulfite sequencing (WGBS). Femora were chosen because of their

742 abundance in present-day human samples, as well as in ancient DNA samples[5,6,59]. In addition,
743 we collected 53 publicly available partial skeletal methylation maps.

744 *WGBS of two modern human bones*

745 **Sample collection**

746 Trabecular bone tissue from femur heads were taken from two patients with osteoarthritis during
747 a total hip replacement surgery, and after filling in a consent form as per Helsinki approval
748 #0178-13-HMO. Importantly, the effects of osteoarthritis processes on trabecular bone are much
749 less substantial than those on the synovium, cartilage, and subchondral bone. Bone1 was a left
750 head of femur taken on August 11, 2014 from a 66 years old female and Bone 2 was a right head
751 of femur taken on September 2, 2014 from a 63 years old female.

752 **DNA Extraction**

753 DNA was extracted from bones using QIAamp® DNA Investigator kit (56504, Qiagen). Bones
754 were cut to thin slices (0.2-0.5 mm) and then thoroughly washed (X5) with PBS, to clean
755 samples from blood. Bones were crushed with mortar and pestle in liquid nitrogen, and 100 mg
756 bone powder was taken to extract DNA according to the protocol "Isolation of Total DNA from
757 Bones and Teeth" of the DNA Investigator kit.

758 **WGBS**

759 Whole-genome bisulfite sequencing was conducted at the Centre Nacional d'analysis Genomico
760 (CNAG) as described in[60]. After cell sorting, genomic DNA libraries were constructed using the
761 Illumina TruSeq Sample Preparation kit (Illumina) following the manufacturer's standard
762 protocol. DNA was then exposed to two rounds of sodium bisulfite treatment using the EpiTect
763 Bisulfite kit (QIAGEN), and paired-end DNA sequencing was performed using the Illumina Hi-
764 Seq 2000. We used the GEM mapper[61] with two modified versions each of the human (GRCh37)

765 and viral reference genomes: one with all C's changed to T's and another with all G's changed to
766 A's. Reads were fully converted in silico prior to mapping to the modified reference genomes,
767 and the original reads were restored after mapping. Although methylation state should not
768 depend on read position, positional biases have been previously reported[62]. We observed that the
769 first few bases from each read showed a slightly higher probability of being called as methylated,
770 and we thus trimmed the first ten bases from each read (M-bias filtering).. Heterozygous
771 positions, positions with a genotype error probability greater than 0.01, and positions with a read
772 depth greater than 250 were filtered out. Only cytosines with six or more reads informative for
773 methylation status were considered. On average, half of the reads from either strand will be
774 informative for methylation status at a given position, so minimum coverage is typically greater
775 than 12. Methylated and unmethylated cytosine conversion rates were determined from spiked-in
776 bacteriophage DNA (fully methylated phage T7 and unmethylated phage lambda). Five samples
777 were excluded based on conversion rates <0.997, supported by visual inspection of CG and non-
778 CG methylation plots. The over-conversion rates for all samples based on methylated phage T7
779 DNA were ~5%.
780 Sequence quality was evaluated using FastQC software v0.11.2. TRIMMOMATIC v.0-32 was
781 used to filter low quality bases with the following parameters: -phred33 LEADING:30
782 TRAILING:30 MAXINFO:70:0.9 MINLEN:70. Paired-end sequencing reads were mapped to
783 bisulfite converted human (hg19) reference genome using Bismark v0.14.3 and bowtie2 v2.2.4
784 not allowing multiple alignments and using the following parameters: --bowtie2 --non_bs_mm --
785 old_flag -p 4. Potential PCR duplicates were removed using Bismark's
786 deduplicate_bismark_alignment_output.pl Perl program. Bismark's
787 bismark_methylation_extractor script was used to produce methylation calls with the following

788 parameters: -p --no_overlap --comprehensive --merge_non_CpG --no_header --bedGraph --
789 multicore 2 --cytosine_report. Examination of the M-bias plots led us to ignore the first 5 bp of
790 both reads in human samples (Extended Data Fig. 5). Custom scripts were used to summarize
791 methylation levels at CpG sites based on the frequencies of methylated and unmethylated
792 mapped reads on both strands. Methylation data were deposited in NCBI's Gene Expression
793 Omnibus and are accessible through GEO accession number GSE96833.

794 *Partial skeletal and full non-skeletal DNA Methylation maps of modern humans and*
795 *chimpanzees*

796 Osteoblast RRBS map, extracted from the femur, tibia, and rib bones of a 6-year-old female
797 (NHOst-Osteoblasts by Lonza Pharma, product code: CC-2538, lot number: 6F4124), was
798 downloaded from GEO accession number GSE27584. 48 450K methylation array maps,
799 extracted from the femora of adult males and females with osteoarthritis or osteoporosis, were
800 downloaded from GEO accession number GSE64490. Four 450K methylation array maps,
801 extracted from unspecified bones of adult males and females were downloaded from GEO
802 accession number GSE50192. Chimpanzee and human WGBS blood methylation maps were
803 downloaded from NCBI SRA accession number SRP059313. Chimpanzee and human WGBS
804 brain maps were downloaded from GEO accession number GSE37202.

805 *Bisulfite-PCR of human bone*

806 **Sample collection**

807 A skull of an adult male from India was obtained from the teaching anatomy collection of the
808 Department of Anatomy and Anthropology at the Sackler Faculty of Medicine, Tel Aviv
809 University, Israel (Human 1). Additional two skull specimens (Human 2 and 3) were obtained
810 directly from the operating room of the Department of Neurosurgery, Shaare Zedek Medical

811 Center, Jerusalem, Israel and transferred on dry ice for further analysis. All study participants
812 provided informed consent according to an institutional review board – approved protocol
813 (SZMC 0048-18).

814 **DNA extraction**

815 Human 1: Standard precautions to avoid contamination were taken, including wearing disposable
816 coats, masks, hair covers and double gloves. All following steps were performed in a UV cabinet
817 dedicated for the preparation of ancient bone samples and located in a physically separated
818 ancient DNA laboratory at the Faculty of Dental Medicine. The skull was cleaned with an excess
819 of 10% bleach (equal to 0.6% Sodium hypochlorite) and then subjected to UV radiation for 30
820 minutes. The cortical layer on the temporal surface (*facies temporalis*) of the zygomatic bone
821 (ZB) was removed by low-speed drilling using a Wolf Multitool Combitool Rotary Multi
822 Purpose Tool equipped with a sterile dental burr. Another sterile burr was used to obtain powder
823 of the subcortical trabecular bone within the body of the zygoma. The powder was collected onto
824 a 10 x 10 cm aluminum foil sheet pretreated with a 10% bleach solution and then transferred into
825 a sterile 1.5 ml Eppendorf tube for subsequent DNA extraction. Altogether, three samples were
826 obtained: ZB-3 from the right zygoma weighing 20.3 mg, and ZB-3/1 and ZB-3/2 from the left
827 zygoma weighing 29.5 mg and 30.3 mg, respectively. Bone DNA was purified from the three
828 bone powder samples using QIAamp DNA Investigator Kit (QIAgen, 56504) according to
829 manufacturer's instructions.

830 Human 2 and 3: DNA was extracted from bones using QIAamp® DNA Investigator kit (56504,
831 Qiagen). Bones were thoroughly washed (X5) with PBS, to clean samples from blood. Bones
832 were crushed with mortar and pestle in liquid nitrogen, and 100 mg bone powder was taken to

833 extract DNA according to the protocol "Isolation of Total DNA from Bones and Teeth" of the
834 DNA Investigator kit.

835 **Bisulfite-PCR**

836 Genomic DNA was bisulfite converted with the EZ DNA Methylation – Lightning Kit (Zymo
837 Research, D5030) according to the manufacturer's instructions. Specifically, each bone sample
838 was bisulfite converted using 500ng as genomic DNA input for the conversion.
839 Bisulfite treated DNA were amplified with the FastStart High Fidelity PCR System (Sigma,
840 03553400001) using the primers listed in Extended Data Table 12. PCR conditions were
841 performed according to manufacturer's instructions and PCR products were visualized on a 1.5
842 % agarose gel. Prior to cloning, PCR products were purified with Gel/PCR DNA Mini Kit (RBC,
843 YDF100) and quantified with a NanoDrop 2000 spectrophotometer.

844 **Cloning and sequencing**

845 CloneJET PCR Cloning Kit (Thermo Scientific, K1231) was used to clone the purified PCR
846 products into a pJET1.2/blunt Cloning Vector following the Blunt-End Cloning Protocol
847 described in the manufacturer's instructions. 5µl of each cloning reaction product were used for
848 transformation of DH5α Competent Cells (Invitrogen, 18265017). Colonies were grown
849 overnight on LB plates containing 100µg/ml ampicillin. Positive transformants were picked and
850 grown overnight in liquid LB medium containing 100 µg/ml ampicillin. Subsequently, plasmid
851 minipreps were purified with a RBC Miniprep Kit (YPD100) according to manufacturer's
852 instructions. Purified plasmids were quantified with a NanoDrop 2000 spectrophotometer and
853 sequenced on an Applied Biosystems 3730xl Genetic Analyzer (Extended Data Fig. 3a,b).

854 **Human primary chondrocyte validation**

855 Primary chondrocyte cultures were obtained from osteoarthritis (OA) donors in accordance with
856 Hadassah Medical Center Institutional Review Board approval and in accordance with the
857 Helsinki Declaration of ethical principles for medical research involving human subjects. End-
858 stage OA patients, with a Kellgren and Lawrence OA severity score of 3-4 were recruited
859 following receipt of a formal written informed consent (n=8; 75% female, mean age 73±7.2
860 years; mean body mass index 30.1 ±5.4 kg/m^2). Hyaline articular cartilage was dissected and
861 human chondrocytes isolated using 3 mg/mL Collagenase Type II (Worthington Cat #
862 LS004177) in DMEM medium (Sigma-Aldrich, St Louis, MI) containing 10% FCS and 1%
863 penicillin-streptomycin (Beit-Haemek Kibutz, Israel), 37°C, 24h incubation. Isolated cells were
864 filtered through a nylon cell strainer (40mm diameter), washed three times with PBS and plated
865 at 1.5 million cells per 14 cm^2 tissue culture dish (passage 0, passage 2). Cells were cultured in
866 standard incubation conditions (37°C, 5% CO_2) until confluence. Chondrocyte DNA purification
867 was performed using GenElute™ Mammalian Genomic DNA Miniprep Kit (Sigma, G1N350).

868 ## Chimpanzee bone DNA methylation maps

869 Overall, we produced six methylation maps from bones of six common chimpanzee (*Pan*
870 *troglodytes*) individuals. They include one WGBS of a wild chimpanzee, one RRBS of an infant
871 chimpanzee, and four 850K methylation arrays of captive chimpanzees.

872 **Ethics Statement**

873 Chimpanzee tissue samples included in this study were opportunistically collected at routine
874 necropsy of these animals. No animals were sacrificed for this study, and no living animals were
875 used in this study.

876 *WGBS of a chimpanzee bone*

877 **Sample collection**

878 We used a rib bone of a 47-year-old female Chimpanzee provided from the Biobank of the
879 Biomedical Primate Research Centre (BPRC), The Netherlands. The postmortem interval was
880 approximately 10-12 hours. The bone was collected during the necropsy procedure and
881 immediately frozen and stored at –80 ºC.

882 **DNA extraction**

883 DNA was extracted in a dedicated ancient DNA laboratory at the Institute of Evolutionary
884 Biology in Barcelona, where no previous work on great apes has ever been conducted. Standard
885 precautions to avoid and monitor exogenous contamination such as frequent cleaning of bench
886 surfaces with bleach, use of sterile coveralls, UV irradiation and blank controls were taken
887 during the process. 200 mg of bone powder were obtained by drilling and the sample was
888 extracted following the Dabney et al. (2013) method[63]. A final 25 µL of extract volume was used
889 for genome sequencing.

890 **WGBS**

891 Analysis was performed similarly to Bone1 and Bone2, with the exception that the BSreads were
892 mapped to bisulfite converted chimpanzee (panTro4) reference genome, and we ignored the first
893 5bp of read1 and the first 44 bp of read2 in the chimpanzee sample (Extended Data Fig. 6).
894 Methylation data were deposited in NCBI's Gene Expression Omnibus and are accessible
895 through GEO accession number GSE96833.

896 *RRBS of a chimpanzee bone*

897 **Sample collection**

898 We used two unidentified long bone fragments that belonged to a newborn wild chimpanzee
899 infant who died during a documented infanticide event at Gombe National Park on 9 March
900 2012. The infant was known to be the offspring of a chimpanzee called Eliza and was partially

901 eaten by an adult female and her family. The sample was collected from the ground about 48
902 hours after the infant's death and stored in RNAlater solution until arrival at Arizona State
903 University (ASU). At ASU the sample was stored at 4°C until extraction.

904 **DNA Extraction**

905 Sampling and DNA extractions were conducted at the ASU Ancient DNA Laboratory, a Class
906 10,000 clean-room facility in a separate building from the Molecular Anthropology Laboratory.
907 Precautions taken to avoid contamination included bleach decontamination and UV irradiation of
908 tools and work area before and between uses, and use of full body coverings for all researchers.
909 The bone samples were pulverized together in December 2012 using a SPEX CertiPrep Freezer
910 Mill. Three DNA extractions were conducted using 50-100 mg of bone powder (Extended Data
911 Table 9) and following the extraction protocol by Rohland and Hofreiter[64]. Two extraction blank
912 controls were included to monitor contamination of the extraction process. One µL each of the
913 sample extract and the blank control were used for fluorometric quantification with the Qubit 2.0
914 Broad Range assay. All extracts were combined for a total volume of 345 µL and approximately
915 0.652 µg of total DNA.

916 **RRBS**

917 RRBS libraries were generated according to Boyle *et al.*[65]. 100-200 ng genomic DNA was
918 digested with MspI. Subsequently, the digested DNA fragments were end-repaired and
919 adenylated in the same reaction. After ligation with methylated adapters, samples with different
920 adapters were pooled together and were subjected to bisulfite conversion using the EpiTect
921 Bisulfite kit (QIAGen) per the manufacturer's recommendations with the following
922 modification: after first bisulfite conversion, the converted DNA was treated with sodium
923 bisulfite again to guarantee that conversion rates were no less than 99%. Two third of bisulfite

924 converted DNA was PCR amplified and final RRBS libraries were sequenced in an Illumina
925 HiSeq 2000 sequencer (Extended Data Table 10). Methylation data were deposited in NCBI's
926 Gene Expression Omnibus and are accessible through GEO accession number GSE96833.

927 *850K DNA methylation arrays*

928 **Sample collection**

929 Four chimpanzee cadavers from captive colonies at the Southwest National Primate Research
930 Center in Texas were used. Femora were opportunistically collected at routine necropsy of these
931 animals and stored in -20°C freezers at the Texas Biomedical Research Institute after dissection.
932 These preparation and storage conditions ensured the preservation of skeletal DNA methylation
933 patterns.

934 **DNA extraction**

935 Samples were then transported to ASU and DNA was extracted from the femoral trabecular bone
936 using a phenol-chloroform protocol optimized for skeletal tissues [66]. From the distal femoral
937 condyles, trabecular bone was collected using coring devices and pulverized into bone dust using
938 a SPEX SamplePrep Freezer/Mill. Specifically, bone cores were obtained from a transverse
939 plane through the center of the medial condyle on the right distal femur, such that the articular
940 surface remained preserved. Cortical bone was removed from these cores using a Dremel
941 (Extended Data Table 11). Tissue collections were performed at the Texas Biomedical Research
942 Institute, and DNA extractions were conducted at the ASU Molecular Anthropology Laboratory.

943 **Genome-Wide DNA Methylation Profiling**

944 Genome-wide DNA methylation was assessed using Illumina Infinium MethylationEPIC
945 microarrays. These arrays analyze the methylation status of over 850,000 sites throughout the
946 genome, covering over 90% of the sites on the Infinium HumanMethylation450 BeadChip as

947 well as an additional 350,000 sites within enhancer regions. For each sample, 400 ng of genomic
948 DNA was bisulfite converted using the EZ DNA Methylation™ Gold Kit according to the
949 manufacturer's instructions (Zymo Research), with modifications described in the Infinium
950 Methylation Assay Protocol. These protocols were conducted at the ASU Molecular
951 Anthropology Laboratory. Following manufacturer guidelines (Illumina), this processed DNA
952 was then whole-genome amplified, enzymatically fragmented, hybridized to the arrays, and
953 imaged using the Illumina iScan system. These protocols were conducted at the Texas
954 Biomedical Research Institute. These array data have been deposited in NCBI's Gene Expression
955 Omnibus and are accessible through GEO Series accession number GSE94677.

956 **Methylation Data Processing**

957 Raw fluorescent data were normalized to account for the noise inherent within and between the
958 arrays themselves. Specifically, we performed a normal-exponential out-of-band (Noob)
959 background correction method with dye-bias normalization to adjust for background
960 fluorescence and dye-based biases and followed this with a between-array normalization method
961 (functional normalization) which removes unwanted variation by regressing out variability
962 explained by the control probes present on the array as implemented in the minfi package in R [67]
963 which is part of the Bioconductor project. This method has been found to outperform other
964 existing approaches for studies that compare conditions with known large-scale differences [67],
965 such as those assessed in this study.

966 After normalization, methylation values (β values) for each site were calculated as the ratio of
967 methylated probe signal intensity to the sum of both methylated and unmethylated probe signal
968 intensities. These β values range from 0 to 1 and represent the average methylation levels at each

969 site across the entire population of cells from which DNA was extracted (0 = completely
970 unmethylated sites, 1 = fully methylated sites).

971 $$\beta \text{ Value} = \frac{\text{Methylated Signal}}{(\text{Methylated Signal} + \text{Unmethylated Signal})}$$

972 Every β value in the Infinium platform is accompanied by a detection p-value, and those with
973 failed detection levels (p-value > 0.05) in greater than 10% of samples were removed from
974 downstream analyses.
975 The probes on the arrays were designed to specifically hybridize with human DNA, so our use of
976 chimpanzee DNA required that probes non-specific to the chimpanzee genome, which could
977 produce biased methylation measurements, be computationally filtered out and excluded from
978 downstream analyses. This was accomplished using methods modified from [68]. Briefly, we used
979 blastn to map the 866,837 50bp probes onto the chimpanzee genome (Assembly: Pan_tro_3.0,
980 Accession: GCF_000001515.7) using an e-value threshold of e^{-10}. We only retained probes that
981 successfully mapped to the genome, had only 1 unique BLAST hit, targeted CpG sites, had 0
982 mismatches in 5bp closest to and including the CpG site, and had 0-2 mismatches in 45bp not
983 including the CpG site. This filtering retained 622,819 probes.
984 Additionally, β values associated with cross-reactive probes, probes containing SNPs at the CpG
985 site (either human or chimp), probes detecting SNP information, probes detecting methylation at
986 non-CpG sites, and probes targeting sites within the sex chromosomes were removed using the
987 minfi package in R [67]. This filtering retained a final set of 576,505 probes.

988 *Bisulfite-PCR of chimpanzee cranial bones*

989 **Sample collection**

990 Postmortem frontal skull bones from two different chimpanzees (chimpanzee 1 and chimpanzee
991 2) were provided by the Biomedical Primate Research Centre (BPRC, The Netherlands). Bones

992 were opportunistically collected during routine necropsy of these animals and stored at -80°C.
993 Chimpanzee 3 and chimpanzee 4 samples were obtained from the chimpanzee cranial collection
994 in the Department of Paleoanthropology in the Senckenberg Research Institute Frankfurt (DPSF)
995 and Natural History Museum Frankfurt [69]. These two chimpanzee specimens are owned by the
996 Justus Liebig University Gießen.

997 **DNA extraction**

998 *Chimpanzee 1 and chimpanzee 2*

999 For each sample, bone powder was obtained by crushing the bones with mortar and pestle.
1000 Approximately 100mg bone powder were used to extract DNA using the QIAamp DNA
1001 Investigator Kit (Qiagen) following manufacturer's instructions.

1002 *Chimpanzee 3 and chimpanzee 4*

1003 Cochlear bone powder was obtained by accessing the petrous bone from the cranial base[70]. DNA
1004 was extracted from about 50 mg of powder according to the protocol described by[63], but adapted
1005 for the use of High Pure Nucleic Acid Large Volume columns (Roche) instead of the Zymo-Spin
1006 V column (Zymo Research) MinElute silica spin column (Qiagen) combination.

1007 **Bisulfite-PCR**

1008 Genomic DNA was bisulfite converted with the EZ DNA Methylation – Lightning Kit (Zymo
1009 Research, D5030) according to the manufacturer's instructions. Specifically, each bone sample
1010 was bisulfite converted two times in parallel using 500ng as genomic DNA input for the
1011 conversion.

1012 3µl of bisulfite treated DNA were amplified with the FastStart High Fidelity PCR System
1013 (Sigma, 03553400001) using the primers listed in Extended Data Table 12. PCR conditions were
1014 performed according to manufacturer's instructions and PCR products were visualized on a 1.5

1015 % agarose gel. Prior to cloning, PCR products were purified with homemade SPRI beads
1016 (chimpanzee 1 and 2) and Gel/PCR DNA Mini Kit (RBC, YDF100, chimpanzee 3 and 4), and
1017 quantified with a NanoDrop 2000 spectrophotometer.

1018 **Cloning and sequencing**

1019 CloneJET PCR Cloning Kit (Thermo Scientific, K1231) was used to clone the purified PCR
1020 products into a pJET1.2/blunt Cloning Vector following the Blunt-End Cloning Protocol
1021 described in the manufacturer's instructions. 3µl (chimpanzee 1 and 2) and 3µl (chimpanzee 3
1022 and 4) of each cloning reaction product were used for transformation of DH5α Competent Cells
1023 (Invitrogen, 18265017). Colonies were grown overnight on LB plates containing 100µg/ml
1024 ampicillin. Positive transformants were picked and grown overnight in liquid LB medium
1025 containing 100 µg/ml ampicillin. Subsequently, plasmid minipreps were purified with a QIAprep
1026 Miniprep Kit (Qiagen, chimpanzee 1 and 2), and RBC Miniprep Kit (YPD100, chimpanzee 3
1027 and 4) according to manufacturer's instructions. Purified plasmids were quantified with a
1028 NanoDrop 2000 spectrophotometer and sequenced on an Applied Biosystems 3730xl Genetic
1029 Analyzer (Extended Data Fig. 3a,b).

1030 Reconstructing ancient DNA methylation maps

1031 La Braña 1 genome sequencing

1032 In a dedicated clean room at Harvard Medical School, powder was extracted from the root of a
1033 lower third molar of the Mesolithic La Braña 1 individual (5983-5747 calBCE (6980±50 BP,
1034 Beta-226472)), from which a non-UDG-treated library was previously sequenced to 3.5x
1035 coverage[8]. Two UDG-treated libraries from the same individual were later generated and
1036 enriched for approximately 1.2 million single targeted polymorphisms and sequenced to an
1037 average of 19.5x coverage at these positions [9]. In this study, we carried out shotgun sequencing

1038 of one of the same UDG-treated libraries from this individual on a NextSeq500 instrument using
1039 2 x 76bp paired end sequences [71]. Following the mapping protocol described previously [9], we
1040 trimmed adapter sequences, only processed read pairs whose ends overlapped by at least 15 bp
1041 (allowing for one mismatch) so that we could confidently merge them, and then mapped to the
1042 human reference sequence hg19 using the command samse in BWA (v0.6.1). We removed
1043 duplicated sequences by identifying sequences with the same start and stop position and
1044 orientation in the alignment, and picking the highest quality one. After restricting to sequences
1045 with a map quality of MAPQ ≥ 10, and sites with a minimum sequencing quality (≥20), we had
1046 an average coverage measured at the same set of approximately 1.2 million single nucleotide
1047 polymorphism targets of 23.0x. This data is available under GEO accession number: GSE96833,
1048 with raw reads deposited under SRA accession number: SRX3194436.

1049 **I1583 Genome sequencing**

1050 In a dedicated clean room at the University College Dublin, powder was extracted from the
1051 cochlear portion of the petrous bone of individual I1583 (archaeological ID L14-200) from the
1052 site of Barcın Höyük in the Yenişehir Plain of the Marmara Region of Northwest Turkey. The
1053 Neolithic individual came from a community that practiced farming, and was anthropologically
1054 determined to be a male aged 6-10 years at the time of death (the sex was confirmed genetically).
1055 The direct radiocarbon date was 6426-6236 calBCE (7460±50 BP, Poz-82231). In a dedicated
1056 clean room at Harvard Medical School, a UDG-treated library was prepared from this powder,
1057 which was previously enriched for about 1.2 million SNP targets, sequenced to 13.5x average
1058 coverage, and published in [9]. We shotgun sequenced the same library on nine lanes of a
1059 HiSeqX10 sequencing with 100bp paired reads. On data processing, we merged overlapping read
1060 pairs, trimmed Illumina sequencing adapters, and dropped read pairs that did not have sample

1061 barcodes (up to 1 mismatch) or cannot be unambiguously merged. We then aligned merged reads
1062 with BWA against human reference genome GRCh37 (hg19) plus decoy sequences, and
1063 combined all nine lanes of data and removed duplicate molecules, achieving an average of 24.3x
1064 coverage evaluated on the 1.2 million targets. This data is available under GEO accession
1065 number: GSE96833, with raw reads deposited under SRA accession number: SRX3194436.

1066 **The reconstruction procedure**

1067 Reconstruction of DNA methylation maps was performed on the genomes of the following
1068 individuals: Ust'-Ishim[6], Loschbour[7], Stuttgart[7], La Braña 1, I1583, and the Vindija
1069 Neanderthal[5], as well as on the previously published Altai Neanderthal and the Denisovan
1070 (Extended Data Table 1). The Vindija Neanderthal reads were downloaded from the Max Planck
1071 Institute for Evolutionary Anthropology website:
1072 http://cdna.eva.mpg.de/neandertal/Vindija/bam/. Only the UDG-treated portion of the genome
1073 (B8744) was used. Additional UDG-treated ancient human full genomes have been published to
1074 date; however, these were sequenced to a relatively low coverage (<5x), and thus, only crude
1075 methylation maps could be reconstructed from them. C→T ratio was computed for every CpG
1076 position along the hg19 (GRCh37) human genome assembly, for each of the samples, as
1077 previously described[4].
1078 In order to exclude from the analyses positions that potentially represent pre-mortem C→T
1079 mutations rather than post-mortem deamination, the following filters were applied: (i) Positions
1080 where the sum of A and G reads was greater than the sum of C and T reads were excluded. (ii)
1081 For genomes that were produced using single-stranded libraries (i.e., Ust'-Ishim, Altai
1082 Neanderthal, Denisovan, Vindija Neanderthal and ~1/3 of the Loschbour library), positions
1083 where the G→A ratio on the opposite strand was greater than 1/(average single strand coverage)

1084 were excluded. This fraction represents a threshold of one sequencing error allowed per position.
1085 For Loschbour, this was performed only on the fraction of reads that came from the single
1086 stranded library. (iii) For all genomes, positions with a C→T ratio > 0.25 were discarded. For the
1087 Vindija Neanderthal, this threshold was raised to 0.5, due to its relatively low coverage (~7x).
1088 (iv) Finally, a maximum coverage threshold of 100 reads was used to filter out regions that are
1089 suspected to be PCR duplicates.
1090 In all genomes, excluding Vindija, a fixed sliding window of 25 CpGs was used for smoothing of
1091 the C→T ratio. This allowed for an unbiased scanning of differentially methylated regions
1092 (DMRs) that is not affected by the size of the window. Due to its relatively low coverage, we
1093 extended the sliding window used on the Vindija genome to 50 CpGs. This extended window is
1094 not expected to introduce a bias, as this genome was not used for DMR detection, but only for
1095 subsequent filtering that was applied equally to all genomes (see later).
1096 As previously described, C→T ratio was translated to methylation percentage using linear
1097 transformation determined from two points: zero C→T ratio was set to the value 0%
1098 methylation, and mean C→T ratio in completely methylated (100% methylation) CpG positions
1099 in modern human bone reference (hereinafter μ_{100}) was set to the value 100% methylation.
1100 Positions where C→T ratio > μ_{100} were set to 100% methylation. For genomes that were
1101 extracted from bones, the modern Bone 2 WGBS map, which is the one with the higher coverage
1102 between the two WGBS modern bone maps, was used to determine μ_{100}. For genomes that were
1103 extracted from teeth, there was no available modern reference methylation map, and therefore,
1104 we transformed the C→T ratio into methylation percentage based on the assumption that the
1105 genome-wide mean methylation is similar to bone tissue. Thus, the genome-wide mean C→T
1106 ratio represents 75% methylation, which is the genome-wide mean of measured methylation in

1107 the Bone 2 reference map. This was accomplished by setting μ_{100} to 1.33 x mean genome-wide
1108 C→T ratio.

1109 DMR detection

1110 The DMR detection algorithm is comprised of five main steps. We hereby provide an overview
1111 of the algorithm followed by a detailed description of each step. The overall goal of this pipeline
1112 is to detect differential methylation, assign it to the lineage on which it arose and filter out
1113 within-lineage variation.

1114 Overview

1115 Step 1: Two-way comparisons. To avoid artifacts that could potentially be introduced by
1116 comparing DNA methylation maps that were produced using different technologies, our core
1117 analysis relied on the comparison of the three reconstructed maps of the Altai Neanderthal,
1118 Denisovan, and Ust'-Ishim. Each of the samples was compared to the other two in a pair-wise
1119 manner, as a raw C→T ratio map against a reconstructed methylation map, and vice versa. This
1120 reciprocal comparison insured that the reconstruction process does not introduce biases to one of
1121 the groups. The minimum methylation difference threshold was set to 50%, spanning >50 CpGs.
1122 Step 2: Three-way comparisons. This step classifies to which of the three hominins the DMR
1123 should be attributed. This step is done by overlapping the three lists of DMRs found in Step 1.
1124 For example, a DMR that is detected between the Neanderthal and Ust'-Ishim and also between
1125 the Denisovan and Ust'-Ishim is considered specific to Ust'-Ishim.
1126 Step 3: FDR filtering. Various factors could introduce noise to the reconstruction process,
1127 including the stochasticity of the deamination process, the use of a sliding window, and
1128 variations in read depth within a sample. We ran simulations that mimic the post-mortem

1129 degradation processes of ancient DNA, then reconstructed methylation maps from the simulated
1130 deamination maps and finally compared them to the original map and identified DMRs. Any
1131 differences in methylation levels between the simulated map and the original reference map stem
1132 from noise. Thus, running the same DMR-detection algorithm on the simulated map vs. the
1133 reference map, enables an estimation of the false discovery rate. We set the DMR-detection
1134 thresholds so that FDR < 0.05.
1135 Step 4: Lineage assignment. The chimpanzee methylation maps were used to polarize the DMRs.
1136 For each DMR, methylation levels in the chimpanzee were compared to those of the three
1137 hominin groups. For example, if methylation levels in the chimpanzee samples clustered with the
1138 archaic humans, the DMR was assigned to the AMH lineage.
1139 Step 5: Within-lineage variability filtering. To determine whether a DMR represents an
1140 individual within a group, or is shared by the entire group, we used a total of 67 AMH, archaic
1141 and chimpanzee methylation maps. We used a conservative approach where DMRs in which
1142 methylation levels in one group overlap (even partially) the methylation levels in another group
1143 were discarded. As 59 out of the 67 maps belong to AMHs, our ability to filter out variation
1144 within this group was better, resulting in fewer DMRs along this lineage. Several various
1145 measures were used to ascertain that a DMR along a lineage does not represent a sex-, bone-,
1146 age-, technology or disease-specific DMR.

1147 **DMR-detection algorithm**

1148 We developed an algorithm specifically designed to identify DMRs between a deamination map
1149 and a full methylome reference. Let i enumerate the CpG positions in the genome. In the
1150 deamination map, let t_i be the number of T's at the C position + the number of A's in the
1151 opposite strand at the G position, i.e., it counts the total number of T's that appear in a position

that is originally C, in the context of a CpG dinucleotide. We similarly use c_i to count the total number of C's that appear in a position that is originally C, in the context of a CpG dinucleotide. The C→T ratio is defined as t_i/n_i, where $n_i = c_i + t_i$. Let φ_i and ψ_i (both between zero and one) be the methylation of this position in the reference genome and in the reconstructed one, respectively. If we denote by π the deamination rate, assumed to be constant throughout the genome, and if we assume that deamination of C into T is a binomial process with probability of success $\pi\psi_i$, we get

$$t_i \sim B(n_i, \pi\psi_i). \tag{1}$$

Our null hypothesis is that the ith CpG is not part of a DMR, namely that $\psi_i = \varphi_i$. The alternative hypothesis states that this CpG is part of a DMR. The definition of this statement is that $|\psi_i - \varphi_i| \geq \Delta$, where Δ is some pre-specified threshold. In other words, under the alternative hypothesis we get that $\psi_i \geq \varphi_i + \Delta$ if the site has low methylation in the reference genome, and $\psi_i \leq \varphi_i - \Delta$ if it has high methylation in the reference genome.

Per-site statistic

Let us start with the first option, testing whether $\psi_i \geq \varphi_i + \Delta$ when φ_i is low. A log-likelihood-ratio statistic would be

$$\ell_i^+ = \ln \frac{\Pr\left(t_i \middle| n_i, \pi(\varphi_i + \Delta)\right)}{\Pr(t_i | n_i, \pi\phi_i)} = t_i \left[\ln\left(1 + \frac{\Delta}{\varphi_i}\right) - \ln \frac{1 - \pi(\varphi_i + \Delta)}{1 - \pi\varphi_i}\right] + n_i \ln \frac{1 - \pi(\varphi_i + \Delta)}{1 - \pi\varphi_i}.$$

Similarly, we can test whether $\psi_i \leq \varphi_i - \Delta$ when φ_i is high using the log-likelihood-ratio statistic

$$\ell_i^- = \ln \frac{\Pr\left(t_i \middle| n_i, \pi(\varphi_i - \Delta)\right)}{\Pr(t_i | n_i, \pi\phi_i)} = t_i \left[\ln\left(1 - \frac{\Delta}{\varphi_i}\right) - \ln \frac{1 - \pi(\varphi_i - \Delta)}{1 - \pi\varphi_i}\right] + n_i \ln \frac{1 - \pi(\varphi_i - \Delta)}{1 - \pi\varphi_i}.$$

1171 We used the value $\Delta = 0.5$ for all samples. The value of π, the deamination rate, was estimated
1172 using the overall C→T ratio in CpG positions whose methylation level is 1 in the modern human
1173 Bone 2 WGBS methylation map, after exclusion of putative pre-mortem substitutions, as
1174 described in the "the reconstruction procedure" section (Extended Data Table 1).

1175 *Detecting DMRs*

1176 The statistics ℓ_i^+ and ℓ_i^- quantify how strongly the estimated methylation in position i deviates
1177 from φ_i. Next, we use these values to identify DMRs using the cumulative-sum procedure
1178 explained below. The process is repeated twice: on the statistic ℓ_i^+ to identify DMRs where the
1179 sample has elevated methylation with respect to the reference, and on the statistic ℓ_i^- to identify
1180 DMRs where the sample has reduced methylation with respect to the reference.
1181 For convenience, we explain the cumulative-sum procedure in the context of ℓ_i^+, but an
1182 essentially identical procedure is used for ℓ_i^-. We define a new vector Q^+ by the recursion

1183 $$Q_0^+ = 0, \quad Q_i^+ = \max(Q_{i-1}^+ + \ell_i^+, 0).$$

1184 Under the null hypothesis, ℓ_i^+ has a negative expectation which produces a negative drift that
1185 keeps Q^+ at zero, or close to zero, levels. Under the alternative hypothesis the expectation is
1186 positive, hence the drift over a DMR is positive, leading to an elevation in the values of Q^+.
1187 Therefore, our next step is to find all intervals $[a, b]$ such that $Q_{a-1}^+ = 0$, $Q_{b+1}^+ = 0$, and $Q_i^+ > 0$
1188 for $a \leq i \leq b$. Let Q_m^+ be the maximum value of Q^+ in this interval, where m is the position of
1189 the maximum. Then, the interval $[a, m]$ would be called a putative DMR.
1190 The statistics ℓ_i^+ and ℓ_i^- are affected by the number of observed cytosine reads, and thus have
1191 higher power to detect hypermethylation (i.e., larger number of cytosine reads) vs.
1192 hypomethylation (Extended Data Fig. 2).

1193 *Filtering DMRs*

1194 Of course, Q^+ may increase locally due to randomness, and thus a putative DMR may not reflect
1195 a true DMR. To filter out such intervals, we used two strategies. First, we applied a set of filters
1196 to assure that the putative DMRs have reasonable biological properties. Second, we cleaned the
1197 remaining putative DMRs by applying a false discovery rate (FDR) procedure. In the first
1198 strategy, we applied two filters: (i) Putative DMRs that harbor less than 50 CpG positions, thus
1199 are shorter than twice the smoothing window size, were removed. (ii) To avoid situations where
1200 two consecutive CpG sites whose genomic locations are remote appear on the same DMR, we
1201 modify the vector Q_i^+ as follows. Let $d_{i,j}$ be the distance along the genome (in nucleotides)
1202 between CpG sites i and j. Then, for every site i such that $d_{i,i-1} > \delta$ we set $Q_i^+ = 0$. We used
1203 $\delta = 1000$ nt for all samples.

1204 To further remove putative DMRs that are unlikely to reflect true DMRs, we eliminated all
1205 DMRs where $Q_m^+ < Q_T^+$. Here, Q_m^+ is the maximum value of Q^+ in the interval as defined earlier,
1206 and Q_T^+ is a threshold determined using a false discovery rate (FDR) procedure, see section
1207 "filtering out noise" below.

1208 *Testing the algorithm*

1209 To verify that the approach above results in a low number of false positives, we applied the
1210 procedure to deamination maps, when compared to themselves in the form of reconstructed
1211 methylomes. As expected, we obtained a negligible number of DMRs, ranging between 0.4%
1212 and 1% of the number of DMRs detected between the humans.

1213 **Two-way DMR detection**

1214 In order to avoid artifacts that could potentially be introduced by comparing DNA methylation
1215 maps that were produced using different technologies, our core analysis relied on the comparison

1216 of the three reconstructed maps of the Altai Neanderthal, Denisovan, and Ust'-Ishim. These are
1217 all high-resolution maps that were derived from genomes sequenced to high coverage (Extended
1218 Data Table 1). In particular, the Ust'-Ishim methylome is of exceptional quality due to its high
1219 coverage and deamination rate (Extended Data Table 1). Also, going through the same post-
1220 mortem degradation processes, the Ust'-Ishim cellular composition is likely to be similar to that
1221 of the Neanderthal and Denisovan.
1222 In order for a deamination map to serve as a reference in the comparison, we have transformed
1223 its C→T ratio values into methylation values (see "the reconstruction procedure" section above).
1224 To remove potential bias that could be introduced through the comparison of a reconstructed
1225 methylation map to a deamination map, we ran each two-way comparison twice: once with the
1226 methylation map of sample 1 against the deamination map of sample 2, and once with the
1227 deamination map of sample 1 against the methylation map of sample 2 (Extended Data Fig. 1).
1228 Therefore, the comparison of three genomes required a total of six two-way comparisons: Ust'-
1229 Ishim versus an Altai Neanderthal reference, Ust'-Ishim versus a Denisovan reference, Altai
1230 Neanderthal versus an Ust'-Ishim reference, Altai Neanderthal versus a Denisovan reference,
1231 Denisovan versus Ust'-Ishim reference, and Denisovan versus Altai Neanderthal reference.
1232 Because the DNA of these three individuals was extracted from both sexes, the DMR-detection
1233 algorithm was only applied to autosomes.

1234 **Three-way DMR detection**

1235 In order to identify DMRs where one group of humans (hereinafter, hominin 1) differs from the
1236 other two human groups (hereinafter, hominin 2 and hominin 3), we set out to find those DMRs
1237 that were detected both between hominin 1 and 2, and between hominin 1 and 3. To this end, we
1238 compare the two lists (hominin 1 vs. hominin 2 and hominin 1 vs. hominin 3) and look for

1239 overlapping DMRs, as previously described[4]. An overlapping DMR exists when a DMR from
1240 one list partially (or fully) overlaps a DMR from the second list. Only the overlapping portion of
1241 the two DMRs from the two-lists was taken.

1242 **Filtering out noise**

1243 There are different factors that potentially introduce noise into the reconstruction process. These
1244 include the stochasticity of the deamination process, the use of a sliding window to smooth the
1245 C→T signal, and variations in read depth. In order to account for these factors and estimate noise
1246 levels, we ran simulations that mimic the post-mortem degradation processes of ancient DNA,
1247 then reconstructed methylation maps from the simulated deamination maps and finally compared
1248 them to the original map and identified DMRs.
1249 The simulation process starts with a methylation map, where the measured or reconstructed
1250 methylation at position i is ψ_i and is assumed the true methylation. Given that n_i is the coverage
1251 at this position, we use the binomial distribution (1) to randomly draw t_i – the number of C's that
1252 had become T's through deamination. The resulting t_i's were then used to compute the C→T
1253 ratios for each position, smoothed and filtered using the same sliding window and thresholds
1254 used in the original analysis, and linearly transformed to methylation percentages as explained
1255 above (hereinafter, simulated methylation map, Extended Data Fig. 4a). Any differences in
1256 methylation levels between the simulated map and the original reference map stem from noise.
1257 Thus, running the same DMR-detection algorithm described above on the simulated map vs. the
1258 reference map, enables an estimation of the false discovery rate. We ran these simulations 100
1259 times for each of the three genomes (Altai Neanderthal, Denisovan, Ust'-Ishim) and determined
1260 the values of the Q_T^+ and Q_T^- thresholds (see section "filtering DMRs" above) such that the mean

1261 number of DMRs that are detected in the simulations is < 0.05 the number of real DMRs
1262 detected (i.e., FDR < 0.05).

1263 DMRs separating chimpanzees and humans

1264 To identify DMRs that separate chimpanzees from all human groups (both modern and archaic),
1265 we first compared the chimpanzee WGBS bone methylome to each of two present-day WGBS
1266 maps (those of Bone1 and Bone2). This was done by scanning the chimpanzee map using a
1267 sliding window of 25 CpGs, in intervals of one CpG position. In each window, we counted the
1268 number of methylated and unmethylated reads in each sample, and computed a *P*-value using
1269 Fisher's Exact test. We then computed FDR-adjusted *P*-values for each window, and discarded
1270 windows with FDR > 0.05 or where the mean methylation difference (Δ) was below 0.5. We
1271 then merged overlapping windows. This left 8,040 DMRs between the chimpanzee and Bone1,
1272 and 12,666 DMRs between the chimpanzee and Bone2. Next, we intersected the two lists to
1273 identify DMRs where the chimpanzee differs from the both present-day samples. This left 6,417
1274 DMRs. Lastly, we compared the chimpanzee methylation levels to all other human samples
1275 (modern and archaic) and filtered out DMRs where the chimpanzee is found within the range of
1276 methylation levels observed in humans. To do so, we followed the procedure described in the
1277 "Removing DMRs with high within-group variability" section below. This resulted in 2,031
1278 DMRs that separate chimpanzees and humans.

1279 Determining the lineages where DMRs originated

1280 DMRs where Ust'-Ishim differs from the Neanderthal and the Denisovan could either arose on
1281 the AMH branch, or in the ancestor of Neanderthals and Denisovans. In order to allocate the
1282 DMRs to the branch in which the change occurred, we used the chimpanzee DNA methylation
1283 data.

1284 First, we used the chimpanzee bone WGBS map. We defined the distance of a DMR in hominin
1285 H to chimpanzee as the mean absolute difference in methylation, $d_{H,C} = \sum_{i \in DMR} |\psi_i^H - \psi_i^C|$.
1286 Here, ψ_i^H is the reconstructed methylation at the i'th CpG in hominin H, and ψ_i^C is the measured
1287 methylation in the same site in the chimpanzee. For Ust'-Ishim-specific DMRs, we used the
1288 following procedure: (i) If both archaic humans were closer to the chimpanzee, the DMR was
1289 placed on the AMH branch. (ii) If Ust'-Ishim was closer than both archaic humans to the
1290 chimpanzee, the DMR was placed on the branch of the ancestor of Neanderthals and Denisovans.
1291 (iii) Otherwise, the DMR was discarded. Out of 5,111 Ust'-Ishim-specific DMRs, we could place
1292 1,729 DMRs on the AMH branch and 1,255 on the branch of the ancestor of Neanderthals and
1293 Denisovans. 1,807 Ust'-Ishim-specific DMRs were discarded due to inconclusive lineage
1294 assignment, and 320 had no data in the chimpanzee WGBS map. For Neanderthal-specific
1295 DMRs, we discarded all DMRs where Ust'-Ishim and the Denisovan were not found to be closer
1296 to the chimpanzee than the Neanderthal. Out of 3,107 Neanderthal-specific DMRs, 693 were
1297 placed on the Neanderthal branch, 2,202 were deemed inconclusive and were discarded, and 212
1298 had no data in the chimpanzee WGBS map. Similarly, we discarded Denisovan-specific DMRs
1299 where Ust'-Ishim and Altai Neanderthal were not found to be closer to the chimpanzee than the
1300 Denisovan. Out of 1,461 Denisovan-specific DMRs, 499 were placed on the Denisovan branch,
1301 855 were deemed inconclusive, and for 107 we had no data in the chimpanzee WGBS map.
1302 We next developed a second, stricter, scheme by also using the chimp 850K DNA methylation
1303 arrays datasets. As the probes cover just part of the CpGs in a DMR, we need to adjust the DMR
1304 methylation level in order to allow a meaningful comparison of 850K methylation data to full
1305 methylation maps. If we mark by j the CpGs in a DMR that are covered by 850K methylation
1306 array (which is a subset of all the CpGs in this DMR), and mark their total number by $J =$

1307 $\sum_{j \in DMR} 1$, then the methylation in the DMR as measured by the array is $m = 1/J \cdot$

1308 $\sum_{j \in DMR} \psi_j^{\text{array}}$, where ψ_j^{array} is the methylation level measured at position j in the array. Let

1309 $m_I = \sum_{i \in DMR} \psi_i^{\text{WGBS}}$ be the methylation of this DMR as computed from the full methylation

1310 map, where ψ_i^{WGBS} is the methylation level measured at position i in the full map. Let $m_J =$

1311 $\sum_{j \in DMR} \psi_j^{\text{WGBS}}$ be the methylation as computed from the full methylation map when limited only

1312 to positions j. Then, we correct the array methylation value m to:

$$m' = \min\left(m \cdot \frac{m_I}{m_J}, 1\right). \tag{2}$$

1313 This procedure was applied to DMRs covered by at least one probe (~65% of DMRs). For the

1314 remaining ~35% of DMRs, we only used the WGBS chimpanzee methylome. This approach was

1315 used in parallel with filtering DMRs using the modern human 450K arrays (Extended Data Fig.

1316 1, see next section).

1317 There are pros and cons to each of these approaches. Using more chimpanzee datasets allow for

1318 more informative process. However, 850K methylation array probes are distributed unevenly

1319 across the genome. Although most DMRs are covered by at least one probe (mean number of

1320 probes per DMR: 1.7, median: 1, maximum: 64), many are nonetheless not covered. AMH

1321 On one hand, lineage assignment of DMRs for which we have array data is more robust and less

1322 prone to misclassification. On the other hand, DMRs with array data are more likely to be

1323 filtered out, as there is more power to detect variability. This could potentially alter the genomic

1324 distribution of DMRs. Therefore, we use both approaches throughout the paper. In analyses

1325 where it is important to maintain an unbiased distribution of DMRs we only use the chimpanzee

1326 WGBS map for polarization, and AMH bone WGBS maps for filtering (see next chapter),

1327 whereas in analyses where it is more important to minimize variability, or where we look at

1328 specific DMRs, we use the stricter approach. The chimpanzee RRBS data was adjusted using the
1329 same technique. However, it was not used for lineage assignment, but rather only as a source for
1330 additional information on DMRs. This is because this protocol particularly targets unmethylated
1331 CpGs, and is therefore too biased for lineage assignment.

1332 ### Removing DMRs with high within-group variability

1333 Our three-way DMR detection algorithm above produces a list of DMRs where one of the three
1334 hominins (Ust'-Ishim, Altai Neanderthal or Denisovan) is significantly different from the other
1335 two. However, such DMRs could stem from variability within any of the groups, and in such
1336 cases cannot be regarded as truly differentiating between the human groups. Some variability
1337 may be removed during the process described above, in "Determining the lineages where DMRs
1338 originate", but even DMRs whose origin can be assigned to a particular lineage do not
1339 necessarily represent fixed methylation changes. To filter out regions that are variable within any
1340 of the human groups, or across all of them, we used two approaches. First, we used the two
1341 modern human WGBS maps, and the I1583 reconstructed skull methylation map. DMRs where
1342 the Neanderthal or Denisovan methylation levels were found within the range of modern human
1343 methylation (i.e., Ust'-Ishim, the two WGBS maps and I1583) were discarded. This left 1,530
1344 out of 1,729 Ust'-Ishim-derived DMRs (hereinafter, full AMH-derived DMRs), 1,230 out of
1345 1,255 DMRs where the Neanderthal and Denisovan are both derived, 692 out of 693 full
1346 Neanderthal-derived DMRs, and 496 out of 499 Denisovan-derived DMRs.
1347 The second approach adds to this the 52 450K methylation array samples, as well as the three
1348 reconstructed methylation maps from teeth (i.e., Loschbour, Stuttgart and La Braña 1). As
1349 described above, using also methylation probes for filtering DMRs provides more power, but can
1350 also introduce biases. Thus, this filtering was used for most analyses, except those where

1351 unbiased genomic distribution of DMRs is critical. Probe methylation data was corrected as
1352 described in equation (2). Within AMH- and archaic-derived DMRs, a DMR was deemed fixed
1353 if the Neanderthal and the Denisovan methylation levels both fell outside the range of
1354 methylation across all modern human samples (reconstructed, WGBS and 450K maps).
1355 Similarly, within Neanderthal- and Denisovan-derived DMRs, a DMR was deemed fixed if the
1356 respective hominin fell outside the range of methylation across all modern human samples and
1357 the other archaic hominin. This approach yielded 873 AMH-derived DMRs (hereinafter referred
1358 to as AMH-derived DMRs), 939 archaic-derived DMRs, 570 Neanderthal-derived DMRs, and
1359 443 Denisovan-derived DMRs.
1360 The limited number of archaic human methylation maps introduces asymmetry in our ability to
1361 determine the level of fixation of DMRs along different lineages. Whereas we used dozens of
1362 AMH skeletal samples, we have just a few archaic samples. This provides us with the ability to
1363 better estimate the distribution of methylation values within each DMR in AMH, and thus to
1364 determine how significantly methylation values in other samples deviate from it. To enhance our
1365 ability to estimate variability within archaic human lineages, we added to the analysis the
1366 reconstructed methylation map of the Vindija Neanderthal. The USER-treated portion of this
1367 genome (the portion amenable for methylation reconstruction) was sequenced to a depth of 7x [5].
1368 Therefore, the methylation map that could be reconstructed from this individual has a
1369 considerably lower resolution compared to the other reconstructed maps used in this study
1370 (coverage 19x to 52x). Nevertheless, due to the reduced ability to detect variability along the
1371 archaic human linages, we employed this map for additional variability filtering along these
1372 lineages. DMRs where the Vindija Neanderthal clustered with the other hominins, and not with
1373 the Altai Neanderthal (or not with either of the archaic humans in the archaic-derived DMRs)

1374 were discarded. The number of DMRs mentioned throughout this chapter already includes this
1375 filtering.
1376 A general concern in working with DNA methylation data is that DMRs that are specific to one
1377 group do not necessarily represent an evolutionary change, but rather reflect a characteristic such
1378 as technology used to measure methylation, tissue, sex, disease or age that is shared by
1379 individuals in this group and not by others. We take two complementary approaches to ascertain
1380 that the DMRs we report are not driven by these factors: (a) for the top DMGs, we match the
1381 samples for the above factors and test whether the hypermethylation of AMHs is still observed.
1382 To this end, we compared Ust'-Ishim (adult femur with no known diseases, methylation map
1383 produced using our reconstruction method) to the Vindija Neanderthal (adult femur with no
1384 known diseases, methylation map produced using our reconstruction method), and we also
1385 compared 52 modern human samples (adult femora, methylation array maps) to four chimpanzee
1386 samples (adult femora, methylation array maps). In all cases, AMHs show significant
1387 hypermethylation compared to the matched samples (Extended Data Figure 3c,d, see
1388 "*Comparing SOX9, ACAN, COL2A1, XYLT1, and NFIX methylation between AMH, chimpanzee*
1389 *and Neanderthal femora*" chapter for additional information). (b) throughout the pipeline, we
1390 take only DMRs where one human group clusters completely outside the other groups regardless
1391 of tissue, sex, disease, age or technology. Thus, these factors are unlikely to drive the reported
1392 methylation changes. This approach is particularly useful in AMH-derived DMRs, where each
1393 group of samples (i.e., AMH samples vs. archaic and chimpanzee samples) include both males
1394 and females, juveniles and adults, and they come from femora, ribs, tibia, skulls, and teeth. Thus,
1395 it is unlikely that the DMRs that differentiate these groups reflect variability that stems from
1396 these parameters[72] (Fig. 1a-c). Archaic-derived DMRs and Neanderthal-derived DMRs are also

1397 unlikely to reflect differences in the above parameters, as in these DMRs, the Vindija
1398 Neanderthal sample (adult, femur bone) is clustered with the Altai Neanderthal sample
1399 (juvenile/adult, phalanx), and not with AMHs, where most samples are from femora of adult
1400 females. Denisovan-derived DMRs, on the other hand, are more likely to stem from age or bone
1401 type differences than other types of DMRs. This is because the Denisovan sample is the only
1402 finger bone, and it comes from a child (6-13.5 years) (Extended Data Table 1). Thus, we cannot
1403 rule out the possibility that some of the Denisovan-derived DMRs reflect finger-specific, rather
1404 than lineage-specific methylation patterns. These DMRs could also possibly reflect age-specific
1405 differences, but this is less likely, as the AMH I1583 sample and the chimpanzee 850K samples
1406 are the same age group as the Denisovan (Denisovan: 6-13.5 years old, I1583: 6-10 [9],
1407 chimpanzees: 10-13) but show different methylation patterns than the Denisovan (Extended Data
1408 Table 1, Fig. 1).
1409 Note that we do not generally expect the number of DMRs along a lineage to be proportional to
1410 the length of the lineage, as this number is determined by several factors. First, the statistical
1411 power to detect DMRs depends on coverage and deamination levels. Thus, our ability to detect
1412 DMRs was lowest in the Denisovan, and highest in Ust'-Ishim. Second, the ability to filter out
1413 within-population variability was substantially higher along the AMH lineage, to which most
1414 samples belong. While filtering out such variability, we also exclude variability that exists across
1415 both AMH and archaic populations. This filtering also discards genomic regions that are variable
1416 between sexes, bone types and regions where methylation patterns tend to be more stochastic.
1417 Variability that exists exclusively along the Neanderthal lineage was partially removed using the
1418 Vindija Neanderthal sample, which comes from a different bone (femur vs. phalanx) and age

1419 (adult vs. juvenile/adult). Along the Denisovan-lineage, on the other hand, such variability could
1420 not be filtered out using our array of samples (Fig. 1).
1421 We also repeated the Gene ORGANizer analyses (see "Gene ORGANizer analysis" section) after
1422 removal of 20 DMRs that overlap regions which were shown to change methylation during
1423 osteogenic differentiation[55]. We show that the enrichment of voice-affecting genes holds, and
1424 thus, the differentiation state of cells in the samples is unlikely to explain the results we report.

1425 ## Comparison to previous reports

1426 We have previously reported that compared to present-day humans, the HOXD cluster of genes
1427 is significantly hypermethylated in the Neanderthal and Denisovan samples[4]. Using the new
1428 methylation maps, we show that this observation holds (Extended Data Fig. 4b). Adding
1429 chimpanzee data, we see that similarly to AMHs, chimpanzee samples are also hypomethylated
1430 compared to archaic humans. This suggests that the hypermethylation arose along the archaic-
1431 human lineage. However, we find that the Ust'-Ishim individual is an outlier among modern
1432 humans, and that his methylation levels are closer to the Neanderthal than to modern humans, as
1433 was also shown by Hanghøj et al.[73]. The Neanderthal and Ust'-Ishim individuals are found >2
1434 standard deviations from the mean observed methylation in modern humans. This suggests that
1435 although the Neanderthal is hypermethylated compared to almost all modern humans, she is not
1436 found completely outside modern human variation. The Denisovan, on the other hand, is found
1437 even further away, and significantly outside the other populations. Given this, the HOXD DMR
1438 was classified as Denisovan-derived (Extended Data Table 2). The Ust'-Ishim remains include a
1439 single femur, and to our knowledge, it was not compared morphologically to other humans.
1440 Thus, further analysis is needed in order to determine whether the hypermethylation of the Ust'-
1441 Ishim individual compared to other AMHs is manifested in morphological changes as well.

1442 Moreover, as this DMR is classified as Denisovan-derived, we cannot rule out the possibility that
1443 it is driven to some extent by age or bone type differences.
1444 Compared to the previously reported DMRs[4], in this study we found four times as many AMH-
1445 and archaic-derived DMRs (2,805 full bone DMRs compared to 891) and roughly twice as many
1446 Neanderthal- and Denisovan-derived DMRs (440 and 598 compared to 295 and 307 in the
1447 Denisovan and Neanderthal, respectively). The list of DMRs reported here cannot be directly
1448 compared to our previous list of DMRs because of several key differences in the analysis: (i) The
1449 previous study focused on DMRs that are invariable across tissues, whereas here we focused on
1450 DMRs in skeletal tissues. In the previous study, we were therefore able to extrapolate and find
1451 trends that extend beyond the skeletal system, such as neurological diseases. In this paper we
1452 focus on the skeletal system, hence the different appearance of the body map (Fig. 2b,c). (ii) the
1453 current study used stricter thresholds for DMR detection, including a minimum of 50 CpGs in
1454 each DMR (compared to 10 CpGs previously), and a requirement for physical overlap in the
1455 three-way DMR detection procedure. (iii) In this study, the AMH reference is a reconstructed
1456 ancient map, whereas in the previous study the AMH reference, as well as the other tissues used
1457 for filtering out noise, were mainly cultured cell lines with RRBS methylation maps.
1458 When filtering DMRs along the lines of the previous study by taking only DMRs with low inter-
1459 tissue variability in humans (STD < 10%), we indeed observe similar trends. For example, when
1460 taking AMH-derived DMGs and analyzing their expression patterns using DAVID's tissue
1461 expression tools[74], we found that the brain is the most represented organ, with 51.5% of DMGs
1462 expressed in this organ (x1.28, FDR = 2.6×10^{-4}), and glial cells are the most over-represented
1463 cell type (x20.6, but FDR > 0.05, UP_TISSUE DB, Extended Data Table 3). In fact, the brain is
1464 the only significantly enriched organ in this analysis. Similarly, when analyzing the GNF DB, we

1465 found that the subthalamic nucleus is the most enriched body part (x1.60, FDR = 9.2 x 10^{-4}),
1466 followed by additional brain regions, such as the olfactory bulb (x1.54, FDR = 0.01), globus
1467 pallidus (x1.41, FDR = 0.04), and more (Extended Data Table 3). Similar enrichment patterns of
1468 the brain can be observed when analyzing expression patterns of all AMH-derived DMGs
1469 (Extended Data Table 3). Finally, we also find that similarly to the previous report, these DMRs
1470 are linked to diseases more often (23.1% compared to the genome average of 10.8%, DAVID
1471 OMIM_DISEASE DB[74]).

1472 ## Validation of face and larynx enrichment in Gene ORGANizer

1473 To test whether the enrichment of the face and larynx could be attributed to the fact that the
1474 analyses are based on skeletal tissues, we tested whether the proportion of genes related to the
1475 face, larynx, vocal folds and pelvis within AMH-derived skeleton-related DMGs is higher than
1476 expected by chance. Out of 100 DMRs in genes that affect the skeleton, 31 genes are known to
1477 affect the voice, 34 affect the larynx, 87 affect the face, and 65 affect the pelvis, whereas
1478 genome-wide these proportions are significantly lower (14.2%, 20.2%, 70.0%, 52.4%, $P = 1.0 \times$
1479 10^{-5}, $P = 1.3 \times 10^{-3}$, $P = 2.1 \times 10^{-3}$, P = 0.03, for vocal folds, larynx, face, and pelvis,
1480 respectively, hypergeometric test). For additional validation tests, see main text.
1481 Genes associated with craniofacial features were taken from the GWAS-catalog (version 2019-
1482 04-21), using a threshold of $P < 10^{-8}$. The following features were used: Dental caries, Cleft
1483 palate, Facial morphology, Intracranial volume, Cleft palate (environmental tobacco smoke
1484 interaction), Cranial base width, Craniofacial macrosomia, Facial morphology (factor 1, breadth
1485 of lateral portion of upper face), Facial morphology (factor 10, width of nasal floor), Facial
1486 morphology (factor 11, projection of the nose), Facial morphology (factor 12, vertical position of
1487 sublabial sulcus relative to central midface), Facial morphology (factor 14, intercanthal

1488 width), Lower facial height, Nose morphology, Nose size, Tooth agenesis (maxillary third
1489 molar), Tooth agenesis (third molar), facial morphology traits (multivariate analysis), Lower
1490 facial morphology traits (ordinal measurement), Lower facial morphology traits (quantitative
1491 measurement), Middle facial morphology traits (quantitative measurement), and Upper facial
1492 morphology traits (ordinal measurement). We then tested their overlap with DMGs. Genes
1493 associated with craniofacial features in the GWAS catalog significantly overlapped DMGs
1494 compared to the fraction expected by chance (5.17x, $P = 3.4 \times 10^{-4}$, hypergeometric test). As a
1495 control, we then tested how this 5-fold enrichment compares to non-craniofacial features. We
1496 used blood-related GWAS as a representative of general non-craniofacial GWAS. We extracted
1497 from the GWAS catalog 22 blood-related traits (the same number as extracted for craniofacial
1498 features), by taking the first 22 traits that appear in a search for the term "blood" and applying a
1499 threshold of $P < 10^{-8}$. We then used these genes as a background control for the craniofacial
1500 enrichment. We observed a 3.86x enrichment of DMGs with regard to craniofacial- vs. non-
1501 craniofacial-associated genes ($P = 0.011$, chi-square test).
1502 Additionally, we conducted a permutation test on the list of 129 AMH-derived DMGs that are
1503 linked to organs on Gene ORGANizer, replacing those that are linked to the skeleton with
1504 randomly selected skeleton-related genes. We then ran the list in Gene ORGANizer and
1505 computed the enrichment. We repeated the process 100,000 times and found that the enrichment
1506 levels we observed within AMH-derived DMGs are significantly higher than expected by chance
1507 for the laryngeal and facial regions, but not for the pelvis ($P = 8.0 \times 10^{-5}$, $P = 3.6 \times 10^{-3}$, $P = 8.2$
1508 $\times 10^{-4}$, and $P = 0.115$, for vocal folds, larynx, face and pelvis, respectively, Extended Data Fig.
1509 2b-e).

1510 Potentially, longer genes have higher probability to overlap DMRs. Indeed, DMGs tend to be
1511 longer (148 kb vs. 39 kb, $P = 9.9 \times 10^{-145}$, *t*-test). We thus checked the possibility that genes
1512 affecting the larynx and face tend to be longer than other genes, and are thus more likely to
1513 contain DMRs. We found that length of genes could not be a factor explaining the enrichment
1514 within genes affecting the larynx, as these genes tend to be shorter than other genes in the
1515 genome (mean: 62.5 kb vs. 73.2 kb, $P = 0.001$, *t*-test). Genes affecting the face, on the other
1516 hand, tend to be longer than other genes (mean: 77.1 kb vs. 65.6 kb, $P = 4.6\times10^{-5}$, *t*-test). To
1517 examine if this factor may underlie the enrichment we observe, we repeated the analysis using
1518 only DMRs that are found within promoter regions (5 kb upstream to 1 kb downstream of TSS),
1519 thus eliminating the gene length factor. We found that the genes where such DMRs occur are
1520 still significantly associated with the face ($P = 0.036$, Fisher's exact test). We next repeated the
1521 promoter DMR analysis for all genes and compared the Gene ORGANizer enrichment levels in
1522 this analysis to the genome-wide analysis. We observed very similar levels of enrichment (2.02x,
1523 1.67x, and 1.24x, for vocal folds, larynx, and face, respectively, albeit FDR values > 0.05 due to
1524 low statistical power). Importantly, AMH-derived DMGs also do not tend to be longer than
1525 DMGs on the other branches (148 kb vs. 147 kb, $P = 0.93$, *t*-test). Together, these analyses
1526 suggest that gene length does not affect the observed enrichment in genes affecting the face and
1527 larynx.
1528 Additionally, to test whether cellular composition or differentiation state could bias the results,
1529 we ran Gene ORGANizer on the list of DMGs, following the removal of 20 DMRs that are
1530 found <10 kb from loci where methylation was shown to change during osteogenic
1531 differentiation[55]. We found that genes affecting the voice and face are still the most over-

1532 represented (2.13x, 1.71x, and 1.27x, FDR = 0.032, FDR = 0.049, and FDR = 0.040, for vocal
1533 folds, larynx, and face, respectively, Extended Data Table 4).
1534 We also investigated the possibility that (for an unknown reason) the DMR-detection algorithm
1535 introduces positional biases that preferentially identify DMRs within genes affecting the voice or
1536 face. To this end, we simulated stochastic deamination processes along the Ust'-Ishim, Altai
1537 Neanderthal, and Denisovan genomes, reconstructed methylation maps, and ran the DMR-
1538 detection algorithm on these maps. We repeated this process 100 times for each hominin and
1539 found no enrichment of any body part, including the face, vocal folds, or larynx (1.07x, 1.07x,
1540 and 1.04x, respectively, FDR = 0.88 for vocal folds, larynx, and face). Perhaps most importantly,
1541 none of the other archaic branches shows enrichment of the larynx or the vocal folds. However,
1542 archaic-derived DMGs show over-representation of the jaws, as well as the lips, limbs, scapulae,
1543 and spinal column (Extended Data Fig. 2f, Extended Data Table 4). In addition, DMRs that
1544 separate chimpanzees from all humans (archaic and modern, Extended Data Table 2) do not
1545 show over-representation of genes that affect the voice, larynx, or face, compatible with the
1546 notion that this trend emerged along the AMH lineage. We also sought to test whether the larynx
1547 and vocal folds, which we found to be significantly enriched only along the AMH lineage, are
1548 also enriched when compared to the other lineages. We ran a chi-squared test on the fraction of
1549 vocal folds- and larynx-affecting AMH-derived DMGs (25 and 29, respectively, out of a total of
1550 120 organ-associated DMGs), compared to the corresponding fraction in the DMGs along all the
1551 other lineages (42 for vocal folds, 49 for larynx, out of a total of 275 organ-associated DMGs).
1552 We found that both the larynx and vocal folds are significantly enriched in AMHs by over 50%
1553 compared to the other lineages (1.57x for both, P = 0.0248 and P = 0.0169 for vocal folds and
1554 larynx, respectively).

1555 Furthermore, we added a human bone reduced representation bisulfite sequencing (RRBS) map,
1556 and produced a RRBS map from a chimpanzee infant unspecified long bone (Extended Data
1557 Table 1, see Methods). RRBS methylation maps include information on only ~10% of CpG sites,
1558 and are biased towards unmethylated sites. Therefore, they were not included in the previous
1559 analyses. However, we added them in this part as they originate from a chimpanzee infant and a
1560 present-day human that is of similar age to the Denisovan (Extended Data Table 1), allowing
1561 sampling from individuals that are younger than the rest. Repeating the Gene ORGANizer
1562 analysis after including these samples in the filtering process, we found that the face and larynx
1563 are the only significantly enriched skeletal regions, and the enrichment within voice-affecting
1564 genes becomes even more pronounced (2.33x, FDR = 7.9×10^{-3}, Extended Data Table 4).
1565 We also examined if pleiotropy could underlie the observed enrichments. To a large extent, the
1566 statistical tests behind Gene ORGANizer inherently account for pleiotropy[11], hence the
1567 conclusion that the most significant shared effect of the AMH-derived DMGs is in shaping vocal
1568 and facial anatomy is valid regardless of pleiotropy. Nevertheless, we tested this possibility more
1569 directly, estimating the pleiotropy of each gene by counting the number of different Human
1570 Phenotype Ontology (HPO) terms that are associated with it across the entire body[19]. We found
1571 that DMGs do not tend to be more pleiotropic than the rest of the genome ($P = 0.17$, *t*-test), nor
1572 do differentially methylated voice- and face-affecting genes tend to be more pleiotropic than
1573 other DMGs ($P = 0.19$ and $P = 0.27$, respectively).
1574 Next, we tested whether the process of within-lineage removal of variable DMRs and the
1575 differential number of samples along each lineage biases the Gene ORGANizer enrichment
1576 analysis. To do so, we analyzed the pre-filtering DMRs along each lineage. We detect very
1577 similar trends to the post-filtering analysis, with the laryngeal and facial regions being the most

1578 significantly enriched within AMH-derived DMRs (1.58x, 1.44x and 1.21x-1.31x for the vocal
1579 folds, larynx and different facial regions, respectively, FDR < 0.05), and for archaic-derived
1580 DMRs, we detect no enrichment of the laryngeal region (FDR = 0.16 and FDR = 0.43 for the
1581 vocal folds and larynx, respectively), and the most enriched regions are the face, limbs, and
1582 urethra. With the exception of the urethra, these results are very similar to the results reported for
1583 the filtered DMRs, suggesting that the process of within-lineage removal of variable DMRs and
1584 the differential number of samples along each lineage does not bias the enrichment results.
1585 Overall, we observe that AMH-derived DMGs across all 60 AMH samples are found outside
1586 archaic human variability, regardless of bone type, disease state, age, or sex, and that
1587 chimpanzee methylation levels in these DMGs cluster closer to archaic humans than to AMHs,
1588 suggesting that these factors are unlikely to underlie the observed trends.
1589 Finally, we tested whether the filtering process in itself might underlie the observed trends. To
1590 this end, we re-ran the entire pipeline on Neanderthal- and Denisovan-derived DMGs, while
1591 applying to them all the filters as if they were Ust'-Ishim DMGs. This resulted in substantially
1592 fewer loci (89 for the Neanderthal and 50 for the Denisovan), which limits statistical power, but
1593 can still be used to examine whether there are any trends of enrichment similar to those observed
1594 in AMHs. We found no evidence that the filtering process could drive the enrichment of the
1595 vocal or facial areas: within Neanderthal-derived loci, filtered as if they were Ust'-Ishim-derived,
1596 we found that the vocal folds were ranked only 18th, with a non-significant enrichment of 1.27x
1597 (FDR = 0.815, compared to an enrichment of 2.11x within AMH-derived DMGs). The larynx
1598 was ranked 76th and showed a non-significant depletion of 0.87x (FDR = 0.783), and the face
1599 was ranked 31st, with a non-significant enrichment of 1.09x (FDR = 0.815). Within Denisovan-
1600 derived loci, filtered as if they were Ust'-Ishim-derived, none of the loci were linked to the vocal

1601 folds nor to the larynx (FDR = 0.535 and FDR = 0.834, respectively), and the face was ranked
1602 30th (1.29x, FDR = 0.535, Extended Data Table 4). This test suggests that the filtering process in
1603 itself is very unlikely to underlie the enrichment of the vocal and facial parts within AMH-
1604 derived DMGs.
1605 Next, we applied the Neanderthal/Denisovan filters to the Ust'-Ishim-derived loci. This resulted
1606 in 792 loci. We found that the vocal folds remained the most enriched body part (1.76x, FDR =
1607 0.032), the larynx was marginally significant (1.53x, FDR = 0.0502), and the facial region was
1608 significantly enriched too (e.g., cheek and chin ranked 2nd, 3rd within significantly enriched
1609 body parts, 1.66x and 1.63x, FDR = 0.031 and FDR = 0.013, respectively, Extended Data Table
1610 4). Importantly, we do not rule out the option that extensive regulatory changes in genes related
1611 to vocal and facial anatomy might have occurred along the Neanderthal and Denisovan lineages
1612 as well. Indeed, as we report in Extended Data Fig. 2, parts of the face are enriched within
1613 Archaic-derived DMGs. However, we currently see no substantial evidence supporting this.
1614 Importantly, the link between genetic alterations and phenotypes related to the voice is complex.
1615 Some brain-related disorders (i.e., clinical disorders that affect the brain) result in alterations to
1616 the voice, the mechanism in which is very difficult to pin down. Although the mechanism
1617 leading to voice alterations (either in its pitch, timbre, volume or range) in some of the genes we
1618 report is unknown, many of the disorders are skeletal, suggesting the mechanism is related to
1619 anatomical changes to the vocal tract. Such changes could also affect more primary functions of
1620 the larynx, such as swallowing and breathing. However, the enrichment we observe in Gene
1621 ORGANizer shows these genes were also shown to drive vocal alterations in the disorders they
1622 underlie[11,19]. Voice and speech alterations were also shown to be driven by cultural, dietary and
1623 behavioral changes affecting bite configuration[75]. Here too, these factors are unlikely to underlie

1624 the vocal alterations in the genes we report, as individuals from the same family as the individual
1625 with the disorder, who do not carry the dysfunctional allele, were not reported to present any
1626 vocal phenotypes.
1627 The larynx is an organ which is primarily involved in breathing and swallowing in mammals. In
1628 humans, the larynx is also used to produce complex speech, but not every change to the larynx
1629 necessarily affects speech. Despite these additional functions, the genes reported by Gene
1630 ORGANizer and HPO were specifically associated with voice alterations, directly or indirectly,
1631 suggesting that although they could have additional effects, their effect on the voice is their most
1632 shared function.

1633 ## Computing correlation between methylation and expression

1634 In order to identify regions where DNA methylation is tightly linked with expression levels, we
1635 scanned each DMR in overlapping windows of 25 CpGs (the window used for smoothing the
1636 deamination signal). In each window we computed the correlation between DNA methylation
1637 levels and expression levels of overlapping genes as well as the closest genes upstream and
1638 downstream genes, across 21 tissues[32]. For each DMR, we picked the window with the best
1639 correlation (in absolute value) and computed regression FDR-adjusted *P*-value. DMRs that
1640 overlap windows with FDR < 0.05 were considered to be regions where methylation levels are
1641 significantly correlated with expression levels. 90 such DMRs were found among the skeletal
1642 AMH-derived DMRs, 93 among the archaic human-derived DMRs, 40 among Neanderthal-
1643 derived DMRs, and 19 among Denisovan-derived DMRs.
1644 As no expression data were available for Ust'-Ishim, Bone1 and Bone2, we approximated their
1645 *NFIX* expression level by taking the average of *NFIX* expression from three osteoblast RNA-seq
1646 datasets that were downloaded from GEO accession numbers GSE55282, GSE85761 and

1647 GSE78608. RNA-seq data for chondrocytes was downloaded from the ENCODE project, GEO
1648 accession number GSE78607 and plotted against measured methylation levels in primary
1649 chondrocytes (see "Human primary chondrocyte validation" chapter). Notably, even though the
1650 expression and methylation data come from different individuals, plotting them against one
1651 another positions them only ~one standard deviation from the expression value predicted by the
1652 regression line (Fig. 5b). Future studies providing RNA expression levels for the laryngeal
1653 skeleton and vocal folds might provide further information on the methylation-expression links
1654 of these genes.

1655 ## Studying the function of DMGs

1656 ### Gene Ontology analysis

1657 Gene ontology and expression analyses were conducted using Biological Process and UNIGENE
1658 expression tools in DAVID[74], using an FDR threshold of 0.05.

1659 ### Gene ORGANizer analysis

1660 Similarly to sequence mutations, changes in regulation are likely to be unequally distributed
1661 across different body systems, owing to negative and positive selection, as well as inherent traits
1662 of the genes affecting each organ. Thus, we turned to investigate which body parts are affected
1663 by the DMGs. To this end, we ran the lists of DMGs in Gene ORGANizer[11], which is a tool that
1664 links genes to the organs they affect, through known disease and normal phenotypes. Thus, it
1665 allows us to investigate directly the phenotypic function of genes, to identify their shared targets
1666 and to statistically test the significance of such enrichments. We ran the lists of DMGs in the
1667 ORGANize option using the default parameters (i.e., based on *confident* and *typical* gene-
1668 phenotype associations).

1669 When we ran the list of skeletal AMH-derived DMRs, we found 11 significantly enriched body
1670 parts, with the vocal folds and the larynx being the most enriched parts (x2.11 and x1.68, FDR =
1671 0.017 and FDR = 0.048, respectively). Most other parts belonged to the face (teeth, forehead,
1672 lips, eyelid, maxilla, face, jaws), as well as the pelvis and nails (Fig. 2c,d, Extended Data Table
1673 4). For archaic-derived DMGs, the lips, limbs, jaws, scapula, and spinal column were enriched
1674 (Extended Data Fig. 2f, Extended Data Table 4). The Neanderthal-derived and Denisovan-
1675 derived DMG lists did not produce any significantly enriched organs, but the immune system
1676 was significantly depleted within Neanderthal-derived DMRs (x0.67, FDR = 0.040).
1677 In order to examine whether such trends could arise randomly from the reconstruction method,
1678 we repeated the analysis on the previously described 100 simulations. We ran all simulated
1679 DMGs (4,153) in Gene ORGANizer and found that no enrichment was detected, neither for
1680 voice-related organs (vocal folds: x0.99, FDR = 0.731, larynx: x.1.02, FDR = 0.966, FDR =
1681 0.966), nor for any other organ.

1682 **Overlap with enhancer regions**

1683 To further test whether the AMH-derived DMRs overlap skeletal regulatory regions, we
1684 examined the previously reported 403,968 human loci, where an enrichment of the active
1685 enhancer mark H3K27ac was detected in developing human limbs (E33, E41, E44, and E47)[76].
1686 Each DMR was allocated a random genomic position in its original chromosome, while keeping
1687 its original length and matching the distribution of GC-content and CpG density between the
1688 original and permutated lists. GC-content and CpG density matching was done by matching a
1689 10-bin histogram of the original and permutated lists. This was repeated for 10,000 iterations.
1690 We found that AMH-derived DMRs overlap limb H3K27ac-enriched regions ~2x more often

1691 than expected by chance (610 overlapping DMRs, compared to 312.4±21.7, $P < 10^{-4}$,

1692 permutation test).

1693 SOX9 upstream putative enhancer coordinates used in Fig. 4b were taken from [13,14,23,77,78].

1694 Computing the density of changes along the genome

1695 We computed the density of derived CpG positions along the genome in two ways. First, we

1696 used a 100 kb window centered in the middle of each DMR and computed the fraction of CpGs

1697 in that window which are differentially methylated (i.e., are found within a DMR). Second, for

1698 the chromosome density plots, we did not center the window around each DMR, but rather used

1699 a non-overlapping sliding 100 kb window starting at position 1 and running the length of the

1700 chromosome.

1701 *NFIX, COL2A1, SOX9, ACAN and XYLT1* phenotypes

1702 The vocal tract and larynx affecting genes presented in this paper show involvement in laryngeal

1703 cartilage and soft tissue phenotypic variation. Clinical phenotypes can be of high severity, with

1704 substantial impacts on normal breathing functions, to the point where the cause of death is due to

1705 respiratory distress. *SOX9* and *NFIX* are often associated with laryngomalacia[11,19] (Extended

1706 Data Table 5), a collapse of the larynx due to malformation of the laryngeal cartilaginous

1707 framework and/or malformed connective tissues, particularly during inhalation. Patients with

1708 mutations in *COL2A1* often show backwards displacement of the tongue base[11,19]. Less severe

1709 phenotypes of the reported genes include variation of voice quality in the form of pitch variation

1710 (high in patients suffering from *XYLT1* mutations) and sometimes hoarseness of the voice

1711 (reported for some patients with mutations of *ACAN*, Extended Data Table 5)[11,19]. Whether this is

1712 due to variation of the vocal tract and laryngeal anatomy influenced by the *ACAN* mutation or

1713 due to a scaled down vocal tract size in the case of the *XYLT1* mutation which also causes
1714 primordial dwarfism is not yet clear.

1715 NFIX phenotypes

1716 Skeletal phenotypes that are associated with the Marshall-Smith syndrome were extracted from
1717 the Human Phenotype Ontology (HPO) [19]. Non-directional phenotypes (e.g., irregular dentition)
1718 and phenotypes that are expressed in both directions (e.g., tall stature and short stature) were
1719 removed.
1720 Mutations in *NFIX* have also been linked to the Sotos syndrome. However, *NFIX* is not the only
1721 gene that was linked to this syndrome; mutations in *NSD1* were also shown to drive similar
1722 phenotypes[51]. Therefore, it is less relevant in assessing the functional consequences of general
1723 shifts in the activity levels of *NFIX*. Nevertheless, it is noteworthy that in the Sotos syndrome
1724 too, most symptoms are a mirror image of the Neanderthal phenotype (e.g., prominent chin and
1725 high forehead).

1726 Comparing of SOX9, ACAN, COL2A1, and NFIX expression between AMH and mouse

1727 93 appendicular skeleton samples were used to compare expression levels of *NFIX*, *SOX9*,
1728 *ACAN* and *COL2A1* in human and mouse: 1. Five Human expression array data of iliac bones [79],
1729 downloaded from ArrayExpress accession number E-MEXP-2219. 2. 84 Human expression
1730 array of iliac bones, downloaded from ArrayExpress accession number E-MEXP-1618. 3. Three
1731 Mouse expression array data of femur and tibia bones, downloaded from ArrayExpress accession
1732 number E-GEOD-61146. 4. One Mouse RNA-seq of a tibia bone, downloaded from
1733 supplementary data. Expression values were converted to percentiles, according to each gene
1734 expression level compared to the rest of the genome across each sample (Fig. 5c).

1735 ## Comparing *SOX9, ACAN, COL2A1, XYLT1*, and *NFIX* methylation between AMH,
1736 chimpanzee and Neanderthal femora

1737 To check whether the AMH hypermethylation of *SOX9, ACAN, COL2A1, XYLT1* and *NFIX*
1738 could be a result of variability between bone types, we compared the four chimpanzee femur
1739 850K methylation arrays to the 52 present-day femur 450K methylation arrays. We took probes
1740 within AMH-derived DMRs that appear on both arrays. We found that these genes are
1741 consistently hypermethylated in AMHs (P = 1.6x10^{-7}, t-test), with 38 probes showing >5%
1742 hypermethylation in AMH, whereas only eight probes show such hypermethylation in
1743 chimpanzees (Extended Data Fig. 3d). Therefore, even when comparing methylation from the
1744 same bone, same sex, same developmental stage, measured by the same technology, and across
1745 the same positions, AMH show consistent hypermethylation across all of these DMGs.
1746 Similarly, when comparing the DMRs in *SOX9*, *ACAN*, *COL2A1*, *XYLT1*, and *NFIX* between the
1747 Ust'-Ishim and Vindija Neanderthal samples, the Vindija Neanderthal sample is consistently
1748 hypomethylated compared to the Ust'-Ishim individual (P = 1.2 x 10^{-5}, Extended Data Fig. 3c).
1749 Both of these samples were extracted from femora of adult individuals, and methylation was
1750 reconstructed using the same technology. This suggests that the hypermethylation of AMHs
1751 compared to Neanderthals is unlikely to be driven by age or bone type, and rather reflects
1752 evolutionary shifts.

1753 ## Scanning the SOX9 region for mutations altering NFI binding motifs

1754 To examine whether the changes in regulation of *SOX9* could possibly be explained by changes
1755 in the binding sites of NFI proteins, we searched for the NFI motif [80,81] along the gene body and
1756 the 350 kb upstream region of *SOX9*. We looked for NFI motifs that exist in the genomes of the

1757 Altai and Vindija Neanderthal, as well as in the Denisovan, but were abolished in AMHs. We did
1758 not find any evidence of such substitutions.

1759 Comparison to divergent traits between Neanderthals and AMHs

1760 To further investigate potential phenotypic consequences of the DMGs we report, we probed the
1761 HPO database[19] and compared these HPO phenotypes to known morphological differences
1762 between Neanderthals and modern humans. To compile a list of traits in which Neanderthals and
1763 AMHs differ, we reviewed key sources that surveyed Neanderthal morphology summarized in [12].
1764 We identified traits in which Neanderthals are found completely outside AMH variation, as well
1765 as traits where one group is significantly different from the other, but the distribution of observed
1766 measurements partially overlap. Non-directional traits (i.e., traits that could not be described on
1767 scales such as higher/lower, accelerated/delayed etc.) were not included, as could not be
1768 paralleled with HPO phenotypes. The compiled list included 107 phenotypes, 75 of which have
1769 at least one equivalent HPO phenotype (4.8 on average). For example, the HPO phenotype
1770 Taurodontia (HP:0000679) was linked to the trait "Taurodontia", and the following HPO
1771 phenotypes were linked to the trait "Rounded and robust rib shafts": *Broad ribs* (HP:0000885),
1772 *Hypoplasia of first ribs* (HP:0006657), *Short ribs* (HP:0000773), *Thickened cortex of long bones*
1773 (HP:0000935), *Thickened ribs* (HP:0000900), *Thin ribs* (HP:0000883), *Thoracic hypoplasia*
1774 (HP:0005257). For each skeleton-affecting phenotype, we determined whether it matches a
1775 known morphological difference between Neanderthals and AMHs. For example, *Hypoplastic*
1776 *ilia* (HPO ID: HP:0000946) was marked as divergent because in the Neanderthal the iliac bones
1777 are considerably enlarged compared to AMHs[12]. We then counted for each gene (whether DMG
1778 or not) the fraction of its associated HPO phenotypes that are divergent between Neanderthals
1779 and AMHs. We found that four of the top five most differentially methylated skeletal genes

1780 (*XYLT1*, *NFIX*, *ACAN*, and *COL2A1*) are in the top 100 genes with the highest fraction of
1781 divergent traits between Neanderthals and AMHs (out of a total of 1,789 skeleton-related genes).
1782 In fact, *COL2A1*, which is the top ranked DMR (Extended Data Table 2), is also the gene that is
1783 overall associated with the highest number of derived traits (63) (Extended Data Table 7). This
1784 suggests that these extensive methylation changes are possibly linked to phenotypic divergence
1785 between archaic and AMHs.

1786 ## Data and Software Availability

1787 All methylation data generated in this work have been deposited in NCBI's Gene Expression
1788 Omnibus under GEO accession number GSE96833.

1789

1790 # Extended Data Figures

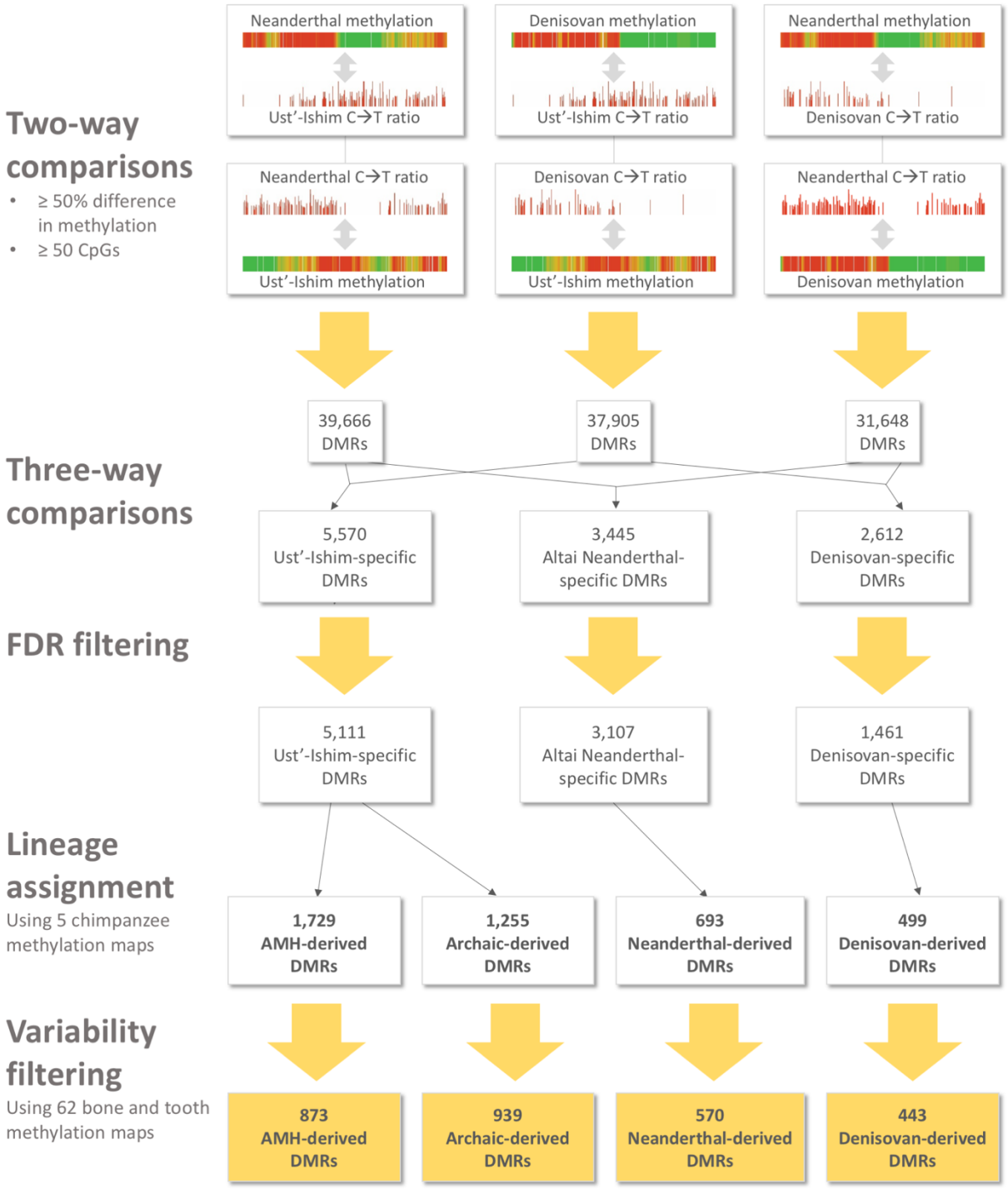

1791

1792 **Extended Data Figure 1. DMR-detection flowchart.** At the core of the process are six two-
1793 way (pairwise) comparisons between the Altai Neanderthal, Denisovan, and Ust'-Ishim
1794 individuals. In each two-way comparison, a C→T deamination signal of one hominin was
1795 compared to the reconstructed methylation map of the other hominin. This resulted in three lists
1796 of pairwise DMRs, that were then intersected to identify hominin-specific DMRs, defined as
1797 DMRs that appear in two of the lists. False discovery rates were controlled by running 100
1798 simulations for each hominin, each simulating the processes of deamination, methylation
1799 reconstruction, and DMR-detection. Only DMRs that passed FDR thresholds of < 0.05 were kept
1800 (see Methods). To discard non-evolutionary DMRs we used 62 skeletal methylation maps, and
1801 kept only loci whose methylation levels differed in one lineage, regardless of age, bone type,
1802 disease or sex. Finally, five chimpanzee methylation maps were used to assign the lineage in
1803 which each DMR likely emerged.

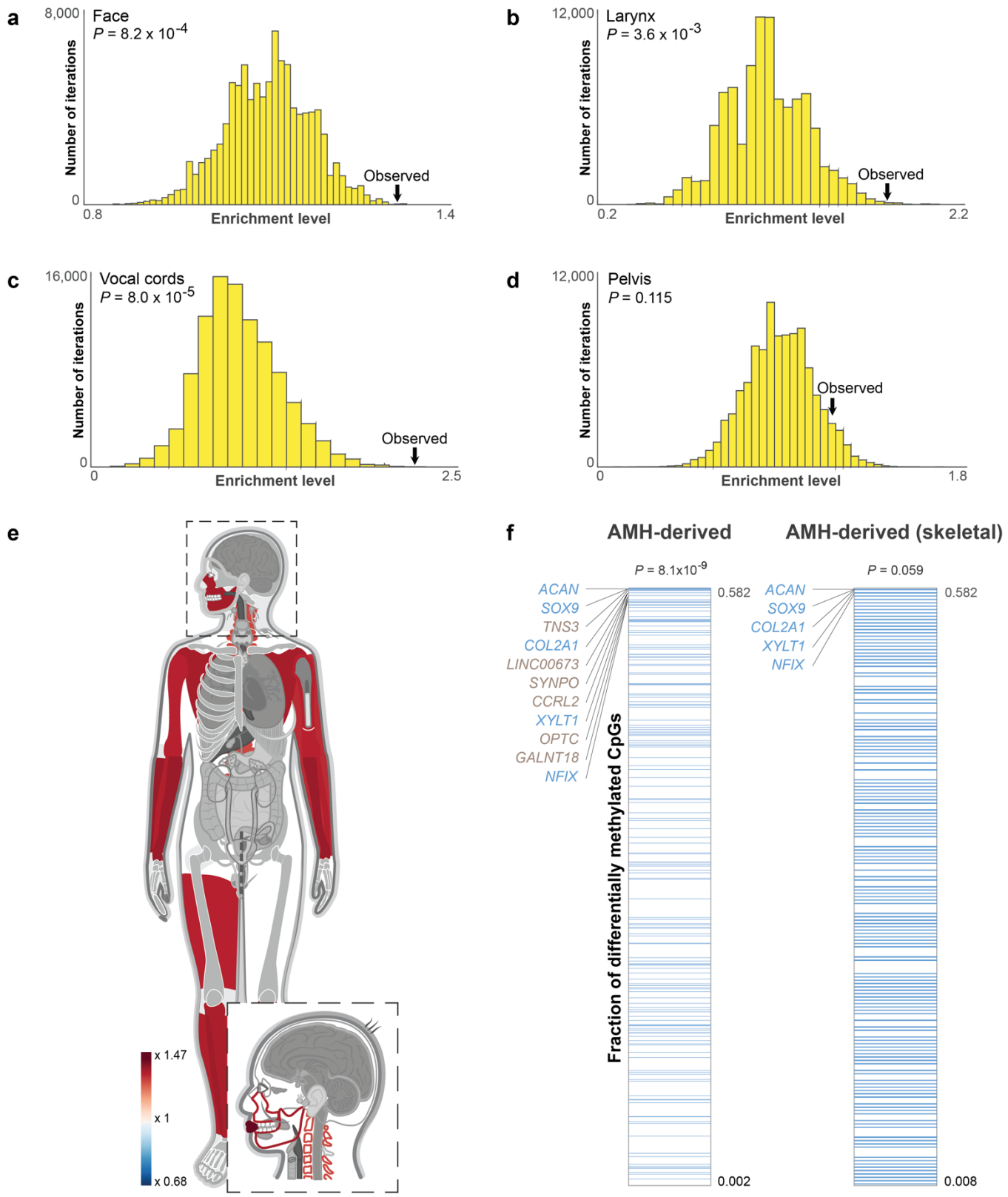
a
Face
P = 8.2 x 10-4
8,000
0
Number of iterations
Observed
0.8
Enrichment level
1.4
b
Larynx
P = 3.6 x 10-3
12,000
0
Number of iterations
Observed
0.2
Enrichment level
2.2
c
Vocal cords
P = 8.0 x 10-5
16,000
0
Number of iterations
Observed
0
Enrichment level
2.5
d
Pelvis
P = 0.115
12,000
0
Number of iterations
Observed
0
Enrichment level
1.8
e
x 1.47
x 1
x 0.68
f
AMH-derived
AMH-derived (skeletal)
P = 8.1x10-9
P = 0.059
ACAN
SOX9
TNS3
COL2A1
LINC00673
SYNPO
CCRL2
XYLT1
OPTC
GALNT18
NFIX
0.582
0.002
ACAN
SOX9
COL2A1
XYLT1
NFIX
0.582
0.008
Fraction of differentially methylated CpGs

1804

1805 **Extended Data Figure 2. The face and larynx are enriched within AMH-derived DMGs**
1806 **compared to genes affecting the skeleton, and compared to archaic-derived DMGs. a-d.** The
1807 distribution of enrichment levels in 100,000 randomized lists of genes, where non-skeletal AMH-
1808 derived DMGs were unchanged, whereas skeleton-related DMGs were replaced with random
1809 skeleton-related genes. Observed enrichment levels are significantly higher than expected in the
1810 face, larynx, and vocal folds. **e.** A heat map representing the level of enrichment of each anatomical
1811 part within archaic-derived DMGs. Genes affecting the lips, limbs, jaws, scapula, and spinal
1812 column are the most enriched within archaic-derived DMRs. Only body parts that are significantly
1813 enriched (FDR < 0.05) are colored. **f.** The number of AMH-derived CpGs per 100 kb centered
1814 around the middle of each DMR. Genes were ranked according to the fraction of derived CpG
1815 positions within them. Genes affecting the face are marked with blue lines. AMH-derived DMGs
1816 which affect the face tend to be ranked significantly higher. Although only ~2% of genes in the
1817 genome are known to affect lower and midfacial projection, three of the top five AMH-derived
1818 DMGs, and all top five AMH-derived skeleton-affecting DMGs affect facial projection.

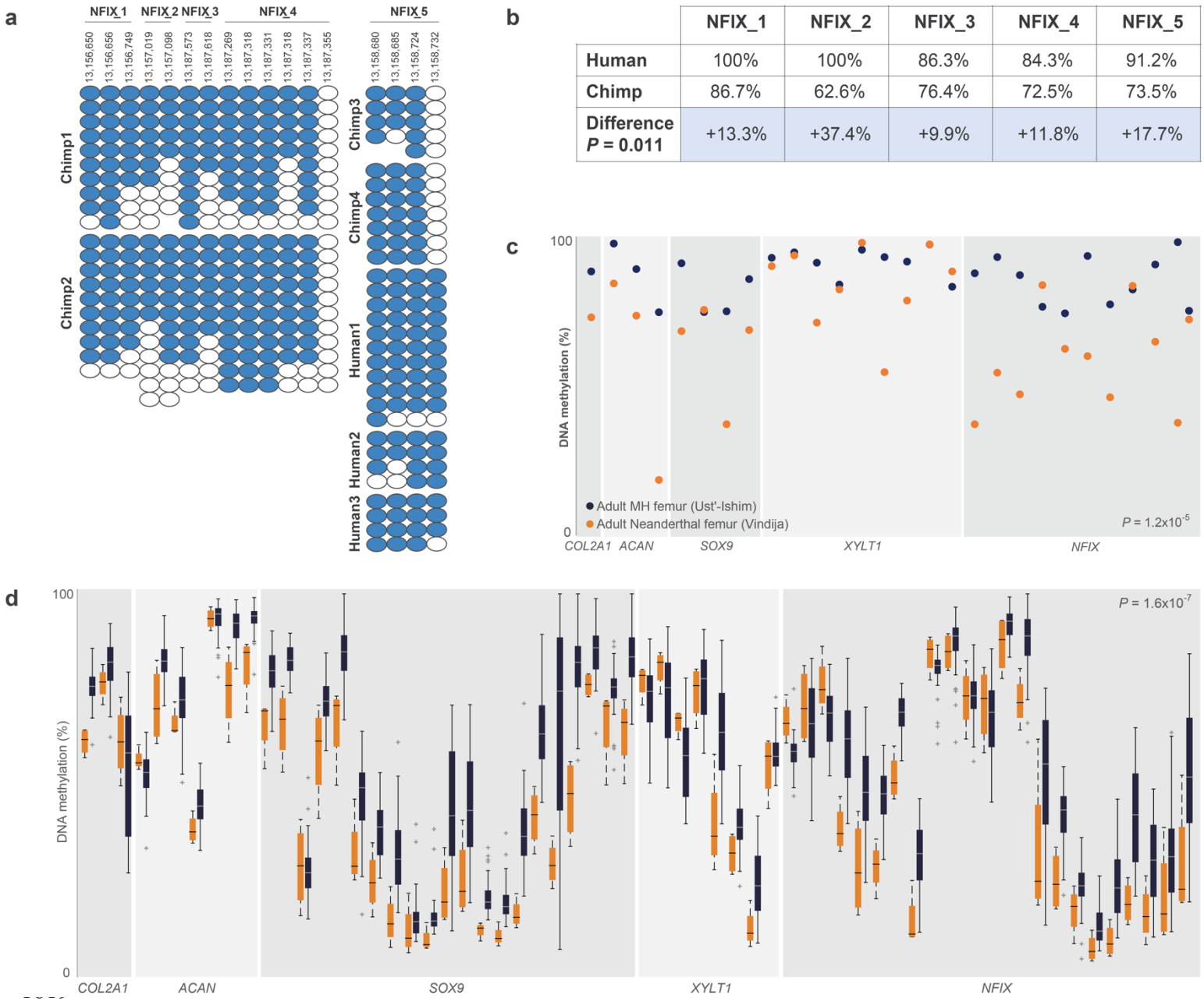

	NFIX_1	NFIX_2	NFIX_3	NFIX_4	NFIX_5
Human	100%	100%	86.3%	84.3%	91.2%
Chimp	86.7%	62.6%	76.4%	72.5%	73.5%
Difference ***P* = 0.011**	+13.3%	+37.4%	+9.9%	+11.8%	+17.7%

Extended Data Figure 3. AMHs are hypermethylated compared to Neanderthal and chimpanzee bone samples, even when age and bone type are considered. a,b. Bisulfite-PCR in human and chimpanzee crania of five regions within the two *NFIX* DMRs, showing hypermethylation of NFIX in AMHs ($P = 0.011$, *t*-test). Each column represents a CpG position, with each circle representing either methylated (blue) or unmethylated (white) measurements. Human hg19 coordinates are shown for each CpG position. Chimpanzee methylation in regions

1826 1-4 was compared with the human I1583 cranium. Region 5 was compared with I1583 and three
1827 additional present-day human crania, presented in the figure. Summarized results are presented
1828 in the table. **c.** *COL2A1, ACAN, SOX9,* and *NFIX* are hypermethylated in Ust'-Ishim (blue)
1829 compared to the Vindija Neanderthal (orange). Circles represent mean methylation levels in
1830 AMH-derived DMRs. Both samples were extracted from femora of adults, and methylation was
1831 reconstructed using the same method. The DMRs presented include also those that were
1832 analyzed in the density analyses (see Methods). The hypermethylation of these genes in AMHs is
1833 unlikely to be attributed to age or bone type. **d.** *COL2A1, ACAN, SOX9,* and *NFIX* are
1834 hypermethylated in AMH femora compared to chimpanzee femora. Each pair of box plots
1835 represents methylation levels across 52 AMH femora (blue) and four chimpanzee femora
1836 (orange) in a single probe of methylation array. When comparing methylation in the same bone,
1837 measured by the same technology, and across the same positions, AMHs show almost consistent
1838 hypermethylation compared to chimpanzee. The probes presented include also probes within
1839 DMRs that were analyzed in the density analyses (see Methods).
1840

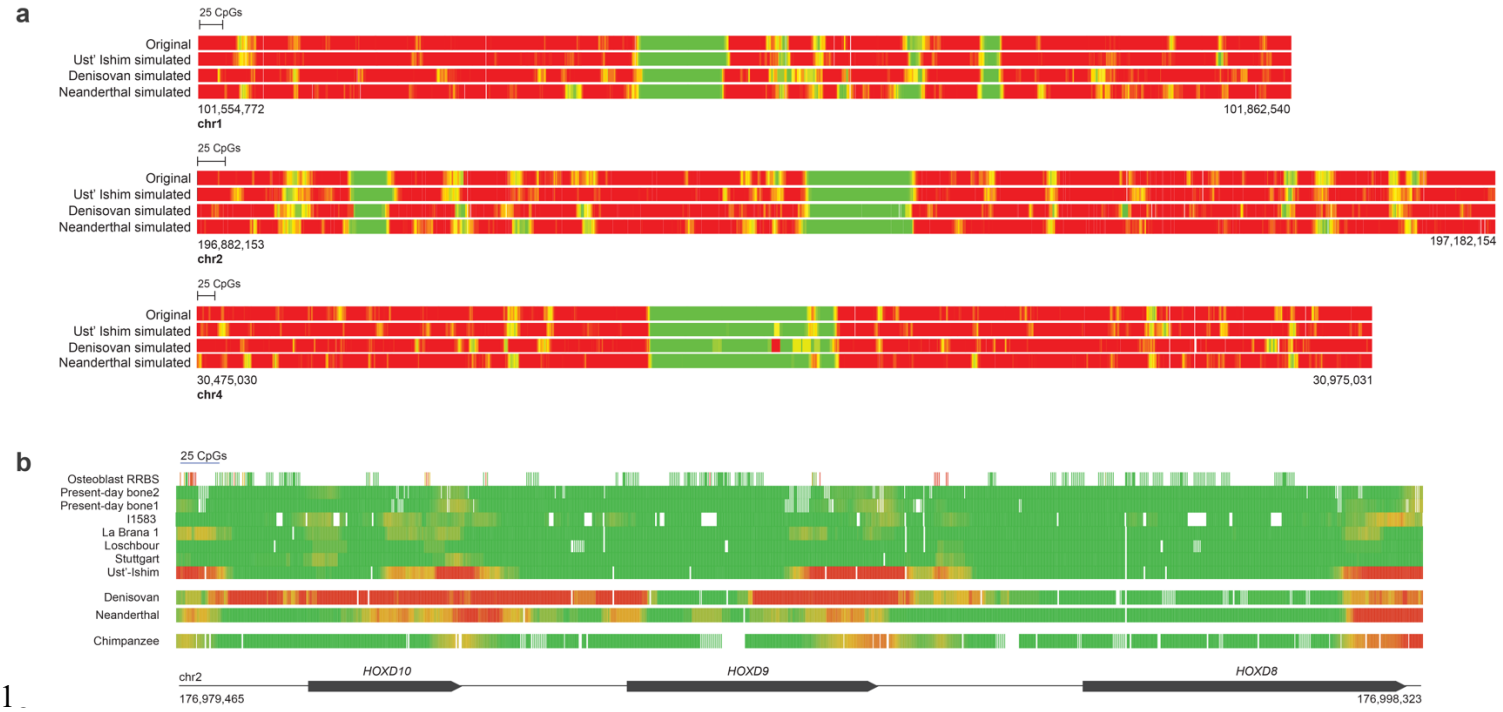

Extended Data Figure 4. Simulations of deamination and reconstruction, and comparison to previous reports. a. Simulations of cytosine deamination, followed by reconstruction reproduce DNA methylation maps. Deamination was simulated for each position based on its methylation level, read coverage and the observed rate of deamination in each hominin. Then, DNA methylation maps were reconstructed and matched against the original map. The number of DMRs found were used as an estimate of false discovery rate. Three exemplary regions are presented, where methylation levels are color-coded from green (unmethylated) to red (methylated). **b.** The HOXD cluster is hypermethylated in archaic humans, and in the Ust'-Ishim individual. Methylation levels are color-coded from green (unmethylated) to red (methylated). The top eight bars show ancient and present-day AMH samples, the lower three show the Denisovan, Neanderthal and chimpanzee. The promoter region of *HOXD9* is hypermethylated in the Neanderthal and the Denisovan, but not in AMHs. The 3' ends of the three genes are

1854 hypermethylated in the Neanderthal, Denisovan, Ust'-Ishim and chimpanzee, but not in other

1855 AMH samples. The promoter of HOXD10 is methylated only in the Denisovan.

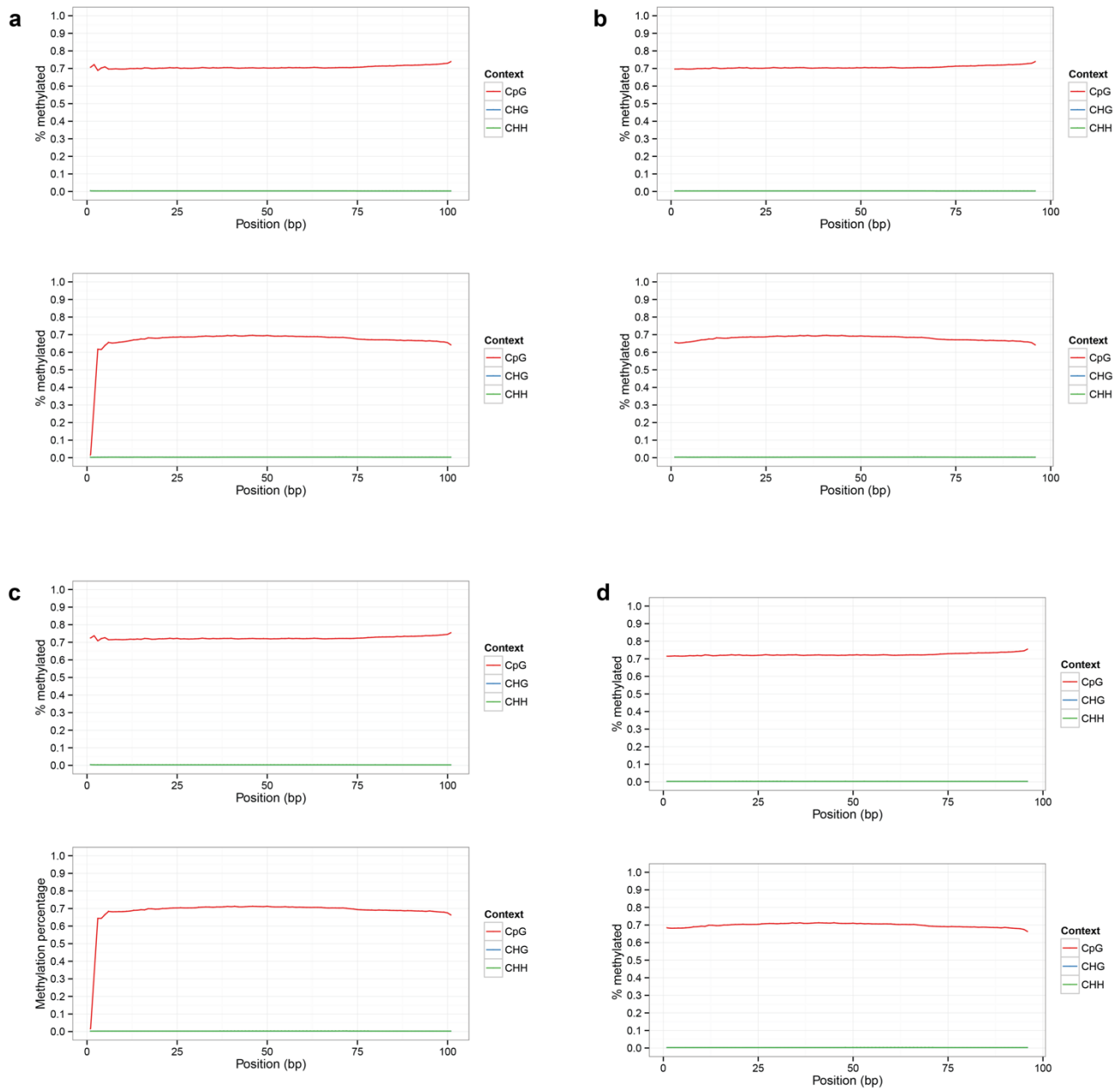

1856

1857 **Extended Data Figure 5**. **M-bias plots along reads in bone sample 1 and sample 2**. **a**. Pre-
1858 filtering methylation along read1 and read2 in the autosomes of bone 1. **b**. Post-filtering
1859 methylation along read1 and read2 in the autosomes of bone 1. **c**. Pre-filtering methylation along
1860 read1 and read2 in the autosomes of bone 2. **d**. Post-filtering methylation along read1 and read2
1861 in the autosomes of bone 2.

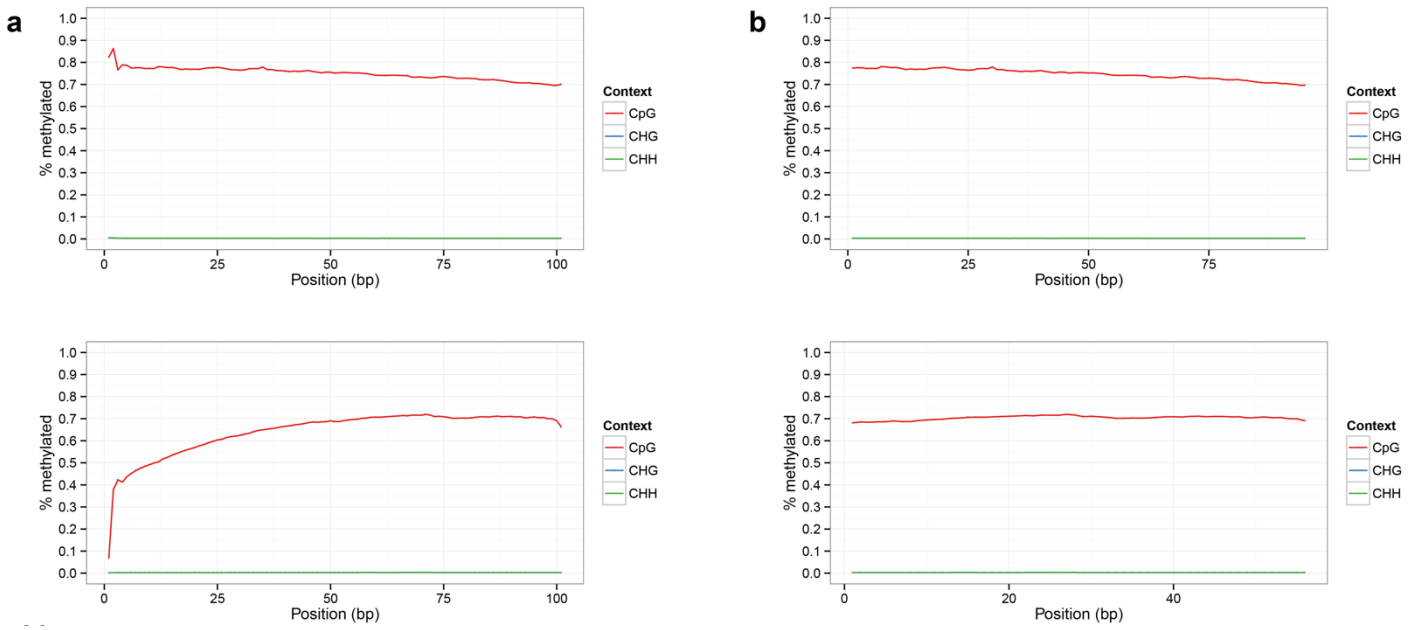

1863 **Extended Data Figure 6**. **M-bias plots along reads in the chimpanzee rib sample**. **a**. Pre-

1864 filtering methylation along read1 and read2 in the autosomes. **b**. Post-filtering methylation along

1865 read1 and read2 in the autosomes.

1866